Imperial College London

Flavour Oscillations in Strong Gravitational Fields

Sam Brady

Supervised by

Dr Katy Clough*

Imperial College London

Department of Physics

Submitted in partial fulfilment of the requirements for the degree of Master of Science of Imperial College London

September 2022

*Queen Mary University of London

Abstract

This dissertation contains the results of new research into flavour oscillations in strong gravitational fields. A new expression has been found for the oscillation probability of flavour-doublet particles escaping from a low-spin Kerr black hole. It has also been shown that an expression used in previous works for scattering by Schwarzschild black holes is still valid in these low-spin cases. A full investigation of flavour oscillations in more general gravitational backgrounds requires an understanding of the 3+1 decomposition of General Relativity, and the advanced techniques of modern numerical relativity. These areas have been introduced, with a focus on the necessary background for the GRChombo numerical relativity code, which has been used here. The results of previous simulations in this area have been reproduced and built upon, with a wide range of parameters tested for comparison with the analytic predictions. These simulations have also been carried out for a Kerr black hole. This work contains all the preliminaries needed for more advanced numerical investigations, where the fixed background assumption no longer holds. An extension can also be made in the future to consider flavour triplet fields.

Acknowledgements

I would like to start by thanking my supervisor Dr Katy Clough for all the help I have been given during this project, and everyone at Queen Mary for being so welcoming this summer.

I would also like to thank Gabriel and Shaun for all their invaluable help across my master's degree, and for making this year a much more enjoyable experience.

Finally I would like to thank Esme, Alex and my parents for all their support this year.

Contents

1 Introduction

1.1 Focus of this work

In this work, the phenomenon of flavour oscillation is investigated in the strong gravitational field surrounding a black hole. This builds on the results obtained in [1], and is inspired by the analytical approximations obtained in both [1, 2]. While flavour oscillations are an interesting phenomenon in their own right, the patterns that have been predicted for oscillating particles scattered by black holes are particularly exciting. As explained in detail later in this work, the oscillation pattern displayed for a simple model of a flavour doublet depends on the absolute masses of the two mass eigenstates. This is particularly important, since neutrinos are the prototypical example of flavour oscillating particles, and their absolute masses are not yet known [3].

The overarching goal of this research is a more complete understanding of the effect of curved spacetimes on flavour oscillations. This will be obtained through both analytic approximations in the 'particle picture' and a number of numerical investigations. An understanding of this effect in general spacetimes will require an exposition of the necessary background, including the 3+1 formulation of General Relativity and the principles of numerical relativity. The first numerical simulations can then be carried out, beginning with a flavour-doublet field scattered by a single non-rotating black hole (allowing for the approximation of a fixed background). A full numerical investigation of more complicated scenarios, such as scattering by binary black hole systems and an extension to full three-flavour neutrino fields, is beyond the scope of this work and will be reserved for future investigations.

The remainder of this introduction is aimed at a wider audience than the following (more technical) work, and will give a qualitative overview of the phenomenon being studied. Section 2 will begin with an brief introduction to the relevant results of General Relativity, before going on to explore the 3+1 decomposition of Einstein's field equations, and the various formulations that work well for numerical simulations. In section 3, analytical approximations of flavour oscillation patters around no- and low-spin black holes will be derived, for comparison with the numerical results in section 5. Before these results are

given, section 4 will describe the numerical methods behind the GRChombo code.
The details given for both the 3+1 formulation and the workings of the numerical code will go beyond what is required to understand the results provided here. This is because these particular simulations are run on a fixed background (i.e., an unchanging metric), which greatly simplifies the equations required and has a negligible effect on their results. However, this deeper analysis will be essential for the development of future work on this topic, where the fixed background assumption will no longer hold.

1.2 Overview of neutrino physics

Flavour oscillations are the result of two things — the wave-like nature of particles, and the 'mixing' (i.e., mismatch) between the mass- and flavour-eigenstates of the oscillating particles. In reality, flavour oscillations are generally considered in terms of neutrinos, which have three distinct flavours. However, a lot of the interesting physics can be captured by a neutrino-*like* particle, with just two flavours. In the particle picture, each neutrino-like particle can be thought of as being built from two fundamental 'types', or flavours. If it is entirely built from one of these flavours, a measurement of its flavour is guaranteed to yield that one result. Otherwise, the result is fundamentally probabilistic, and depends on the relative proportions of the two flavour states it is built from.
Forgetting flavour for a moment, another important parameter that can be measured is the particle's mass. It turns out that this follows the exact same story — each particle can also be considered, with equal validity, as being built from two distinct mass states. The complications arise in combining these two pictures. The key result is that the two fundamental flavour states (or 'bases') are not aligned with the two mass bases. Therefore, if a particle is in one flavour (mass) state, it will be in a combination of mass (flavour) states. The relation between these two bases is well-known[1], and can always be used to change between the two descriptions.
As mentioned above, the other important cause of flavour oscillations is the wave-like nature of particles. Fortunately, the basis states in the mass basis (the mass eigenstates) obey a simple wave equation. This means that, as shown in the top half of figure 1, they

[1]In this two-flavour picture, the bases are related by a simple U(2) rotation — see section 3.1.

oscillate sinusoidally in time (or, equivalently[2], distance along their path).

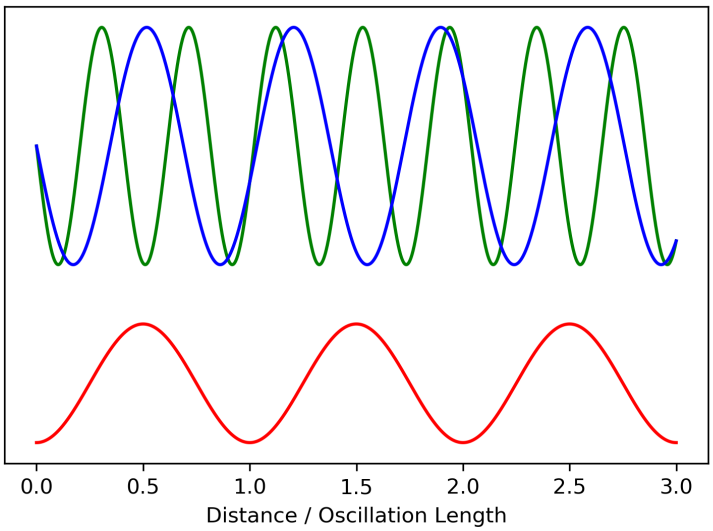

Figure 1: The upper half shows the real parts of two complex waves, corresponding to the propagation of two mass eigenstates. The lower half shows the resulting oscillation probability.

The wavelength of each basis state depends on its mass, so the two mass eigenstates oscillate differently along their shared path. This means that when a measurement is made further along the path, the proportions of the two mass states have changed. As a result, the proportions of the two flavour states (which are built from these mass states) have also changed, and the probability of a change in flavour has changed with them.

1.3 Effects of general relativity

In ordinary Newtonian physics, all processes occur on a fixed three-dimensional Euclidean background, with a universal 'clock' that all observers agree on. This was implicitly assumed in the calculations for figure 1, where the distance travelled along the path was assumed to have a simple 'distance = velocity × time' relation to some observer-independent measure of time.

In Einstein's theory of general relativity, however, space and time are unified into one four-dimensional *spacetime*. In this world, distances and times are no longer agreed on

[2]Assuming particles with constant velocity.

by different observers, and what was considered the force of gravity is now an effect of the geometry of this spacetime. As frequently quoted from John Wheeler, "Spacetime tells matter how to move; matter tells spacetime how to curve." — i.e., the presence of matter changes the geometry of spacetime, and the geometry of spacetime affects the behaviour of matter. The mathematical description of this relationship will be outlined in later sections, but the most relevant features are these: a large concentration of mass into a small area creates extreme curvature of this spacetime; this curvature then affects the paths of particles passing near the mass, and thus affects the probability of flavour oscillations further along those paths.

In all but the most simple cases, the equations that govern this (highly nonlinear) relationship between matter and curvature are not solvable by pen and paper. In these cases the equations are often tackled numerically, using high-performace computing capabilities to approximate the solutions, often to a very high degree of accuracy. To do this, the equations must be put into a form that is both solvable in this way (the 3+1 decomposition of section 2.2), and 'behaves well' in these simulations (such as the CCZ4 formulation of section 2.7). This will be the topic of the following section.

2 General Relativity and the 3+1 Formulation

2.1 General Relativity

Einstein's theory of General Relativity is formulated in the language of differential geometry. Differential geometry gives a mathematical description of manifolds, and tensor fields on them. The brief overview of General Relativity given here will have two key results — the mathematical description of particle motion, which is necessary for the 'particle picture' of flavour oscillations, and the full Einstein field equations. These equations can then be decomposed, allowing for the numerical simulation of flavour oscillations in the 'field picture'. While it is not directly relevant for this work, it is worth noting that the equations of General Relativity can be obtained by employing an action principle, and using the Einstein-Hilbert action (e.g., appendix E of [4]). The reader is assumed to have

a basic knowledge of differential geometry, with an understanding of manifolds, vectors and forms.

2.1.1 The metric

The spacetime metric $g_{\mu\nu}$ is a (0,2) tensor field defined over the whole manifold. As such, it defines a map $\mathcal{T}_p\mathcal{M} \times \mathcal{T}_p\mathcal{M} \rightarrow \mathcal{R}$, taking two vectors defined at a point p and returning a real number. Given two vector fields $u, v \in \mathcal{T}_p\mathcal{M}$, it obeys the conditions $g(u,v) = g(v,u)$, and $g(u,v) = 0\ \forall v \in \mathcal{T}_p\mathcal{M}$ iff $v = 0$. This second condition means that $g_{\mu\nu}$ can always be diagonalised at a point by an appropriate coordinate transformation. In General Relativity, this diagonalised metric will have the signature (-1,1,1,1). The metric defines an inner product between vectors at a point, and therefore the result of the metric acting on two instances of the same vector can be interpreted as the norm of that vector. While the specific components of these vectors depend on the coordinate frame used, the metric tensor allows for vectors v to be categorised by the sign of their norm as timelike; $v_\mu v^\mu < 0$, null; $v_\mu v^\mu = 0$, or spacelike; $v_\mu v^\mu > 0$.

An important application of the metric tensor is in calculating the line element ds, used to define distance s along a curve $\mathcal{C}$ as

$$s = \int_{\mathcal{C}} \sqrt{ds^2} \tag{1}$$

$$ds^2 = dx^\mu dx^\nu g_{\mu\nu}, \tag{2}$$

where both here and above the Einstein summation convention has been assumed.

2.1.2 Differentiation on manifolds

Given just a manifold, $\mathcal{M}$, and the concept of tensors fields, there is no clear way to generalise differentiation beyond the action of vectors on scalar fields. For example, to generalise the concept of differentiation to vector fields, a way to compare neighbouring tangent spaces is required. There are multiple ways to define differentiation on a manifold, and the most important for General Relativity is known as the *covariant derivative*.

The problem of comparing neighbouring tangent spaces can be considered in reverse —

if differentiation is first *defined* (based on some reasonable requirements), it can then be used to identify vectors in neighbouring tangent spaces (known as parallel transport).

It makes intuitive sense that a derivative operator should take a vector field U, defined over (at least) some neighbourhood of the point p, and a specific vector in the tangent space at p, $v \in \mathcal{T}_p\mathcal{M}$, and return another vector that can be interpreted as the derivative of U along v. Denoting this mapping ∇, it is required to be bilinear, local (i.e., not dependent on v_e, the local extension of v around the point p), and obey the Leibniz rule. The frame-dependent connection coefficients $\Gamma^{\mu}_{\alpha\beta}$ are then defined by the action of the connection on the basis vectors, i.e.,

$$\nabla_{e_\alpha} e_\beta = \Gamma^{\gamma}_{\alpha\beta} e_\gamma \tag{3}$$

The infinitesimal displacement vector dl along a curve $\mathcal{C}(\lambda)$ can be defined by its action on a scalar field f, $dl : f \to f(\mathcal{C}(\lambda + d\lambda)) - f(\mathcal{C}(\lambda))$. A vector v is then parallelly transported along $\mathcal{C}$ iff $\nabla_{dl} v = 0$.

The full expression for the covariant derivative of a vector field t is then,

$$\nabla_\mu t^\nu = \partial_\mu t^\nu + \Gamma^{\nu}_{\mu\alpha} t^\alpha \tag{4}$$

which can be extended to other tensor fields by considering the action on a scalar field (a simple partial derivative) and the Leibniz rule.

In General Relativity, the connection preserves the metric, i.e., $\nabla g = 0$, and is torsion free — these requirements then make this choice of connection, known as a Levi-Civita connection, unique (for a proof, see Theorem 4.3.1 of [5]).

The other important notion of differentiation needed here is the *Lie derivative*. As mentioned above, some method of comparing vectors in neighbouring tensor fields is needed to define a derivative of tensors, and the Lie derivative does this by infinitesimally transporting one vector field along the flow defined by another, and comparing its value to the original value it had there.

Writing the flow of a vector field u as Φ, the point p is mapped a small distance ϵ by Φ to the point q, i.e., $q = \Phi_\epsilon(p)$. This map allows for the push-forward of the vector field v at

p, denoted $v(p)$, to the point q — this is written as $\Phi_{\epsilon *}v(p)$. Defining the Lie derivative then as

$$\mathcal{L}_u v = \lim_{\epsilon \to 0} \left(\frac{v(q) - \Phi_{\epsilon *} v(p)}{\epsilon} \right) \tag{5}$$

it is easily shown that, in components,

$$(\mathcal{L}_u v)^\nu = u^\mu \frac{dv^\nu}{dx^\mu} - v^\mu \frac{du^\nu}{dx^\nu} = u^\mu \nabla_\mu v^\nu - v^\mu \nabla_\mu u^\nu = [u, v] \tag{6}$$

As with the covariant derivative, the same requirements allow for a simple extension to general tensors.

2.1.3 Curvature

Given the lack of background to compare to, and the coordinate dependence of all (non scalar) tensors, it is not immediately clear how curvature should be defined. However, since a key feature of curved space is the path-dependence of parallel transport (equivalently, the non-vanishing connection coefficients), curvature can be quantified by the failure of successive covariant derivatives to commute. The resulting tensor is called the Riemann curvature tensor, and can be given by its action on a general vector field ω as,

$$R^\alpha{}_{\beta\gamma\delta}\omega^\beta = [\nabla_\gamma, \nabla_\delta]\omega^\alpha. \tag{7}$$

Two useful quantities are the Ricci tensor, given by the contraction of the Riemann tensor on its first and third indices,

$$R_{\mu\nu} = R^\alpha{}_{\mu\alpha\nu} \tag{8}$$

and the Ricci scalar,

$$R = R_{\mu\nu} g^{\mu\nu} \tag{9}$$

2.1.4 Einstein Field Equations

From the Bianchi identity,

$$\nabla_\alpha R^\mu{}_{\nu\beta\gamma} + \nabla_\gamma R^\mu{}_{\nu\alpha\beta} + \nabla_\beta R^\mu{}_{\nu\gamma\alpha} = 0, \tag{10}$$

repeated contractions with the metric give,

$$\nabla_\mu(R^{\mu\nu} - \frac{1}{2}g^{\mu\nu}R) = \nabla_\mu G^{\mu\nu} = 0 \tag{11}$$

where $G^{\mu\nu}$ defined here is the Einstein tensor. The full Einstein Field equations (in geometric units) are then,

$$G^{\mu\nu} + \Lambda g^{\mu\nu} = 8\pi T^{\mu\nu} \tag{12}$$

where Λ is the cosmological constant, and $T^{\mu\nu}$ is the stress energy tensor containing the contributions from non-gravitational fields.

For a thorough introduction to General Relativity, see for example [4, 6].

2.1.5 Geodesics

As mentioned in the introduction, the curvature of spacetime has a direct effect on the motion of matter. This effect is clearest when a small, 'freely falling' test mass is considered. The world lines (paths through the spacetime manifold) of these test masses follow curves called geodesics. These curves are the generalisation of straight lines to curved space, in that they minimise the distance (see equation (1)) between two points. Geodesic motion therefore generalises Newton's first law to curved space, stating that a body which is unaffected by external forces stays in uniform motion *along a straight line*.

The equation that governs these geodesics can be found in multiple ways. These include minimising equation (1) with the Euler-Lagrange equations[3], or requiring that the tangent vectors to these curves are parallelly transported along themselves, i.e.,

$$\nabla_v v = 0 \tag{13}$$

where $v = \frac{dx^\mu}{d\lambda}$ and λ is an 'affine parameter' for the geodesic. This route directly gives the geodesic equation for curves $x^\mu(\lambda)$,

[3]This method is particularly convenient when generalising to include other, non-gravitational forces

$$\frac{d^2x^\mu}{d\lambda^2} + \Gamma^\mu_{\alpha\beta}\frac{dx^\alpha}{d\lambda}\frac{dx^\beta}{d\lambda} \tag{14}$$

where the connection coefficients $\Gamma^\mu_{\alpha\beta}$ are defined in equation (3).

2.2 3+1 Decomposition

While [7, 8, 9] have all been used to guide the following sections, the final forms of the important equations have been chosen to mirror those in [8]. [8] is therefore the most useful reference for comparisons to this work, and for detailed derivations of the results presented here.

2.2.1 Submanifolds

Informally, the 3+1 decomposition of spacetime is just the separation of the 4-dimensional manifold, with 3 spacelike dimensions and 1 timelike, into a stack of 3-dimensional 'slices', with each point on a given slice having the same time coordinate. Figure 2 gives an illustration of this 'foliation' of spacetime. In the following equations, the Greek letters are assumed to take the values 0 to 4 inclusively, while Latin letters are assumed to represent the (spatial) coordinate labels 1 to 3.

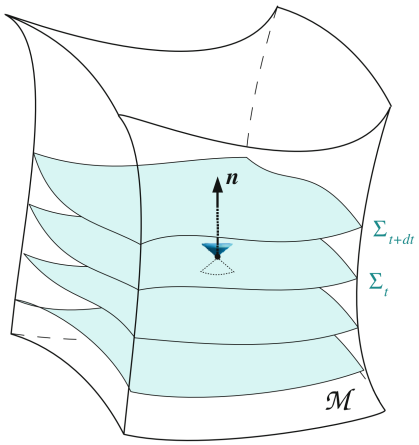

Figure 2: A simple illustration from [8] of spacelike hypersurfaces Σ_t foliating a 2+1 dimensional manifold $\mathcal{M}$, with the normal vector n and its light cone included.

More formally, the *hypersurfaces* (slices) Σ are 3-dimensional manifolds embedded in the

full manifold $\mathcal{M}$. These hypersurfaces are spacelike, which is defined by their normal vector (see below) being timelike everywhere. The maps Φ from Σ into $\mathcal{M}$ allow for the push-forward of vectors into $\mathcal{M}$ and the pull-back of one-forms. In fact, since they are homeomorphisms, the inverse mappings Φ^{-1} also allow for the reverse of these.

To specify this mapping, the first step is to assume the existence of a suitable scalar field t, and then to define the surfaces Σ as level surfaces of t. The normal to these surfaces, n, is proportional to the gradient of t,

$$n_\mu = -\alpha \nabla_\mu t \tag{15}$$

where α may vary. If the scalar field t is used as the time coordinate, the pull-back of vectors and one forms on $\mathcal{M}$ to these surfaces corresponds simply to 'dropping' their time components.

For t to be a valid time coordinate, and therefore for the Σ to be spacial, n must be a timelike vector, and for convenience it is normalised to -1.

The pull-back of the metric g to Σ is called the *induced metric* γ. Since the hypersurfaces Σ are spacelike, γ is non-degenerate, and so a connection D on Σ can be defined analogously to the connection ∇ on $\mathcal{M}$. This connection has a corresponding Riemann tensor $R^i{}_{jkl}$, Ricci tensor R_{ij}, and Ricci scalar R. From here on, these symbols will refer to the tensors on 3-dimensional hypersurfaces, and a superscript ^{4} will specify the 4-dimensional versions.

2.2.2 Curvature revisited

The curvature that is codified by the induced metric is referred to as the *intrinsic* curvature, as it is intrinsic to the embedded hypersurfaces themselves. The other important form of curvature in the 3+1 decomposition is called the *extrinsic* curvature, and relates to the change in the direction of n across Σ. It is a bilinear form, defined for all $u, v \in \mathcal{T}_p\mathcal{M}$ by,

$$K(u, v) = -u \cdot \nabla_v n \tag{16}$$

The trace of the extrinsic curvature, $K = g^{\mu\nu} K_{\mu\nu} = \gamma^{ab} K_{ab}$, is referred to as the *mean curvature*. Using equation (16) and the Lie derivative described in section 2.1.2, the

extrinsic curvature can be re-expressed as the Lie derivative of the 3-metric γ along the normal vector n,

$$K_{\mu\nu} = -\frac{1}{2}\left(\mathcal{L}_n \gamma\right)_{\mu\nu} \tag{17}$$

The *orthogonal projector*, denoted $\vec{\gamma}$, is defined by the map of a vector $v \in \mathcal{T}_p\mathcal{M}$,

$$\vec{\gamma}(v) = v + (n \cdot v)n \tag{18}$$

and in components,

$$\gamma^{\alpha}{}_{\beta} \equiv g^{\alpha}{}_{\beta} + n^{\alpha} n_{\beta} \tag{19}$$

with the α index raised on the spacetime metric by the inverse spacetime metric, giving a tensor which acts as a Kronecker delta.
Using this new tool to express $D_\mu v^\nu$ in terms of $\nabla_\mu v^\nu$,

$$D_\mu v^\nu = \gamma^{\alpha}{}_{\mu}\gamma^{\nu}{}_{\beta}\nabla_\alpha v^\beta \tag{20}$$

allows for the following relation to be shown,

$$D_u v = \nabla_u v + K(u, v)n \tag{21}$$

showing that the extrinsic curvature can also be thought of as the difference between the 4- and 3-dimensional covariant derivatives ∇ and D.

2.2.3 The Gauss and Codazzi relations

The orthogonal projector can now be used to project the components of various equations onto Σ, obtaining relations between these new quantities. First, the analogue of equation (7) for the three-dimensional $R^{\mu}{}_{\nu\alpha\beta}$,

$$R^{\mu}{}_{\nu\alpha\beta} v^\nu = D_\alpha D_\beta v^\mu - D_\beta D_\alpha v^\mu \tag{22}$$

can be fully projected onto Σ, and using equation (21) then gives the Gauss relation;

$$\gamma^{\mu}{}_{\alpha}\gamma^{\nu}{}_{\beta}\gamma^{\gamma}{}_{\rho}\gamma^{\sigma}{}_{\delta}\,{}^{4}R^{\rho}{}_{\sigma\mu\nu} = R^{\gamma}{}_{\delta\alpha\beta} + K^{\gamma}{}_{\alpha}K_{\delta\beta} - K^{\gamma}{}_{\beta}K_{\alpha\delta} \tag{23}$$

Contracting this equation on γ and α and taking its trace then gives the scalar Gauss relation;

$${}^{4}R + 2\,{}^{4}R_{\mu\nu}n^{\mu}n^{\nu} = R + K^{2} - K_{ij}K^{ik} \tag{24}$$

where $K = K^{\mu}{}_{\mu}$.

Second, applying equation (7) to n and projecting the resulting relation onto Σ gives the Codazzi relation,

$$\gamma^{\gamma}{}_{\rho}n^{\sigma}\gamma^{\mu}{}_{\alpha}\gamma^{\nu}_{\beta}\,{}^{4}R^{\rho\sigma}{}_{\mu\nu} = D_{\beta}K^{\gamma}{}_{\alpha} - D_{\alpha}K^{\gamma}{}_{\beta} \tag{25}$$

and again contracting on α and γ gives the contracted Codazzi relation,

$$\gamma^{\mu}{}_{\alpha}n^{\nu}\,{}^{4}R_{\mu\nu} = D_{\alpha}K - D_{\mu}K^{\mu}_{\alpha} \tag{26}$$

Finally, again applying equation (7) to n, but now projecting twice along Σ and once along n, gives the Lie derivative of the extrinsic curvature along $m := \alpha n$,

$$\mathcal{L}_{m}K_{\alpha\beta} = m^{\mu}\nabla_{\mu}K_{\alpha\beta} - 2\alpha K_{\alpha\mu}K^{\mu}_{\beta} - K_{\alpha\mu}D^{\mu}\alpha n_{\beta} - K_{\beta\mu}D^{\mu}\alpha n_{\alpha} \tag{27}$$

Projecting this equation fully onto Σ, and finding that this has no effect on $\mathcal{L}_{m}K_{\alpha\beta}$ (which is tangent to Σ) gives the Ricci equation,

$$\gamma_{\alpha\mu}n^{\rho}\gamma^{\nu}{}_{\beta}n^{\sigma}\,{}^{4}R^{\mu}{}_{\rho\nu\sigma} = \frac{1}{\alpha}\mathcal{L}_{m}K_{\alpha\beta} + \frac{1}{\alpha}D_{\alpha}D_{\beta}\alpha + K_{\alpha\mu}K^{\mu}{}_{\beta} \tag{28}$$

the final non-trivial decomposition of equation (7).

2.2.4 ADM decomposition of the Einstein equations

Einstein's field equation (equation (12)) can now be projected on its two indices, with important equations coming from all of the full projection onto Σ, the full projection along n, and the mixed projection. It is more convenient in some cases to use the trace-reversed form of (12),

$$ {}^4R_{\mu\nu} = 8\pi \left(T_{\mu\nu} - \frac{1}{2} T g_{\mu\nu} \right) \tag{29} $$

where $T := g^{\mu\nu} T_{\mu\nu}$ is the trace of the stress-energy tensor $T_{\mu\nu}$.
First, projecting this form of the Einstein equations fully onto Σ (and using equations (23) and (28)) gives,

$$ \mathcal{L}_m K_{ij} = -D_i D_j \alpha + \alpha \left[R_{ij} + K K_{ij} - 2 K_{ij} K^k{}_j + 4\pi [(S - E)\gamma_{ij} - 2 S_{ij}] \right] \tag{30} $$

where

$$ E := T(n, n) = T_{\mu\nu} n^\mu n^\nu \tag{31} $$

is the stress-energy tensor applied to the normal vector n (equivalently, projected along n) twice, $S_{\mu\nu}$ is the projection onto Σ of the stress-energy tensor,

$$ S_{\mu\nu} = T_{\alpha\beta} \gamma^\alpha{}_\mu \gamma^\beta{}_\nu \tag{32} $$

and $S := g^{\mu\nu} S_{\mu\nu}$ is its trace. The remaining (mixed) projection of $T_{\mu\nu}$ is given by,

$$ p_\mu = -T_{\alpha\beta} \gamma^\alpha{}_\mu n^\beta \tag{33} $$

Second, projecting equation (12) fully along n (and using equation (24)) gives the Hamiltonian constraint,

$$ R + K^2 - K_{ij} K^{ij} = 16\pi E \tag{34} $$

The third and final projection of the Einstein equations is the mixed projection of equation (12), giving (with equation (26)) the momentum constraint,

$$D_i K^i_{\ j} - D_j K = 8\pi p_j \tag{35}$$

Equations (30), (34), and (35) (together with (17)) are often referred to as the ADM equations, and make up a complete reformulation of the Einstein equations. To express these equations as a system of coupled PDEs (partial differential equations), a coordinate system must be chosen. As expected in General Relativity, there is no unique choice for these coordinates, and different choices may favour different physical situations.

Taking the scalar function t to be the time coordinate, the vector ∂_t will in general differ from the vector m defined previously. While the vector m is always perpendicular to the spacial hypersurfaces Σ, the vector ∂_t corresponds to the direction of no change in the x^i coordinates. The difference between these vectors is known as the shift vector $\vec{\beta}$, which lies along Σ and can be interpreted as the freedom to (smoothly) define the coordinate axes on each spacial hypersurface.

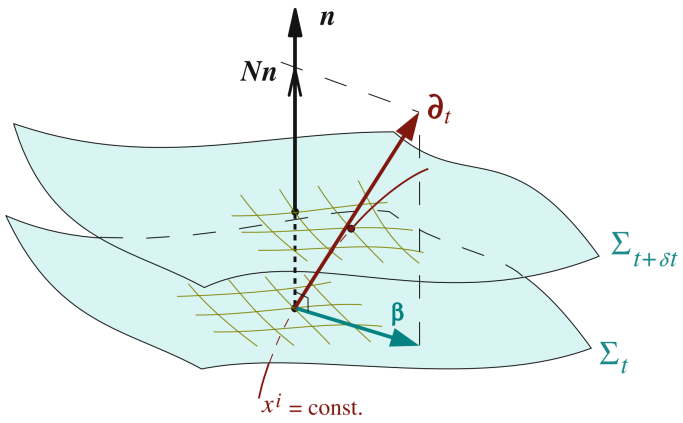

Figure 3: A demonstration of the vectors ∂_t, $m = Nn$ (where $N = \alpha$) and β on a spacial slice, from [8].

The spacetime metric in these coordinates is then,

$$g_{\mu\nu} = \begin{pmatrix} -\alpha^2 + \beta_\alpha \beta^\alpha & \beta_\nu \\ \beta_\mu & \gamma_{ij} \end{pmatrix} \tag{36}$$

Writing the components of β in the x^i directions as β^i, the normal vector n can then be specified as $n = \frac{1}{\alpha}(1, \vec{\beta})$. Also, using that $\partial_t = m + \beta$ (see figure 3), $\mathcal{L}_m$ can be decomposed into $\mathcal{L}_m = \mathcal{L}_{\partial_t} - \mathcal{L}_\beta$.

Furthermore, since

$$(\mathcal{L}_{\partial_t} K)_{ij} = (\partial_t)^a \partial_a K_{ij} + K_{aj} \partial_i (\partial_t)^a + K_{ia} \partial_j (\partial_t)^a = (\partial_t V)^\beta \tag{37}$$

for a general tensor V, and

$$\mathcal{L}_\beta K_{ij} = \beta^a \partial_a K_{ij} + K_{aj} \partial_i \beta^a + K_{ia} \partial_j \beta^a \tag{38}$$

in these coordinates, the LHS of equation (30) can be rewritten as

$$\mathcal{L}_m K_{ij} = \partial_t K_{ij} - \beta^a \partial_a K_{ij} - K_{aj} \partial_i \beta^a - K_{ia} \partial_j \beta^a \tag{39}$$

This completes the decomposition of the Einstein equation into a system of coupled partial differential equations.

2.3 Stress energy tensor of scalar fields

In this work, the only form of matter is a pair of massive scalar fields[4]. The equation of motion for a scalar field ϕ with mass m is the Klein-Gordon equation,

$$\partial_\mu \partial^\mu \phi + m^2 \phi = 0 \tag{40}$$

This can be decomposed (as in [10]) into two first-order differential equations in the vari-

[4]In the numerical simulations presented later, the masses of these fields are low enough that the effect of $T_{\mu\nu}$ on the metric can be neglected.

ables ϕ and $\Pi_M := \mathcal{L}_n\phi$,

$$\partial_t\phi - \beta^i\partial_i\phi = \alpha\Pi_M \tag{41}$$

$$\partial_t\Pi_M - \beta^i\partial_i\Pi_M = \gamma^{ij}(\alpha\partial_i\partial_j\phi + \partial_i\alpha\partial_j\phi) + \alpha\left(K\Pi_M - \gamma^{ij}\Gamma^k_{ij}\partial_k\phi + m^2\phi\right) \tag{42}$$

The stress energy tensor for scalar fields is also needed, and is found from the Klein-Gordon Lagrangian to be

$$T_{\mu\nu} = \nabla_\mu\phi\nabla_\nu\phi - \frac{1}{2}g_{\mu\nu}(\nabla_\rho\phi\nabla^\rho\phi - m^2\phi^2) \tag{43}$$

Once $T_{\mu\nu}$ has been calculated, it can be decomposed (as in section 2.2.4) into the tensors S_{ij}, p_i, S, and E.

2.4 Partial differential equations and hyperbolicity

With the equations of General Relativity fully decomposed in the preceding sections, it may appear that the task of 3+1 decomposition is fully completed. However, it has long been known that the ADM equations are not suitable for use in numerical relativity. The reason for this relates to the 'weak hyperbolicity' of these equations, and will be explored in this section. This discussion follows the arguments made in [7], with a more detailed discussion given in [11].

A general second-order partial differential equation in the variables x and y can be written as[5]

$$A\partial_x^2\phi + B\partial_x\partial_y\phi + C\partial_y^2\phi = f(\phi) \tag{44}$$

where $f(\phi)$ can contain up to first-order derivatives of ϕ. These equations can initially be classified according to the following requirements,

[5]B here is 2 × the B in [7]

$$\text{Equation (44) is} = \begin{cases} \text{Hyperbolic} & \text{if} \quad B^2 - 4AC > 0 \\ \text{Parabolic} & \text{if} \quad B^2 - 4AC = 0 \\ \text{Elliptic} & \text{if} \quad B^2 - 4AC < 0 \end{cases} \tag{45}$$

For the purposes of numerical simulations, hyperbolic equations are very desirable. Elliptic equations require boundary conditions at the spacial edges of the simulation, and only specify data for a given spacial slice. The Hamiltonian constraint (equation (34)) is an elliptic equation. Hyperbolic and parabolic equations, however, require a suitable initial state, but then determine how this state evolves in time.

The desirability of hyperbolic equations is further explained by the notion of 'well-posedness'. All hyperbolic equations can be arranged into the form,

$$\partial_t^2 \phi - v^2 \partial_x^2 \phi = \rho \tag{46}$$

where v is a constant (corresponding to the wave-speed), and ρ may contain up to first-order derivatives of ϕ. This second-order equation can be decomposed into first-order equations in the variables ϕ, $k = -\partial_t \phi$, and $l = \partial_x \phi$. The state of ϕ and its derivatives can be contained in a vector $u = (\phi, k, l)$, and with a source vector $S = (-k, -\rho, 0)$ these first-order equations can be written together as

$$\partial_t u + A \cdot \partial_x u = S \tag{47}$$

where the velocity matrix A is given by,

$$\begin{pmatrix} 0 & 0 & 0 \\ 0 & 0 & v^2 \\ 0 & 1 & 0 \end{pmatrix} \tag{48}$$

By considering equation (47) in an eigenbasis of A, it is clear that the eigenvalues of this velocity matrix correspond to speeds, known as 'characteristic speeds'. These are the speeds with which the components of u in this basis propagate. In spaces with more than 1 spacial dimension, the term $A \cdot \partial_x u$ in equation (47) becomes $A^i \cdot \partial_i u$, and the solution

vector gains additional spacial derivatives.

An equation is considered well-posed if some norm of the solution vector u can be defined that obeys,

$$|u(x,t)| \leq \alpha e^{\beta t}|u(x,0)| \tag{49}$$

for all times t, where α and β are constants. It is clear that this is a necessary (but not always sufficient) requirement for good behaviour in simulations, since solutions that grow faster than exponentially would be greatly undesirable.

To determine which hyperbolic equations obey this condition, it is useful to classify them as weakly, strongly, or symmetric hyperbolic (a subset of strongly hyperbolic equations). Strongly hyperbolic equations (and therefore symmetric hyperbolic also) automatically satisfy condition (49).

In [7], this further classification is carried out by considering a matrix P formed by the product of A^i with an arbitrary unit vector n_i. If, for all possible choices of n_i, the eigenvectors of P are complete (and have real eigenvalues), the equations are strongly hyperbolic. If the eigenvalues are real but the eigenvectors are not complete, they are weakly hyperbolic. Finally, if P can be symmetrised in a way that is independent of n^i (for example by all the M^i being symmetric already), they are symmetric hyperbolic.

As mentioned previously, the ADM equations are only weakly hyperbolic. However, they can be reformulated into systems of equations that are strongly hyperbolic. This will be the topic of the following sections.

2.5 BSSN equations

To make the 3+1 equations strongly hyperbolic, and therefore more suitable for numerical evolution, various changes can be made. In the BSSN formalism, these changes include a conformal rescaling of the metric, and the addition of multiples of the constraint equation. This latter change is automatically allowed by the requirement that the constraint equations be equal to zero everywhere. The conformally related metric is given by,

$$\tilde{\gamma}_{ij} = e^{-4\phi}\gamma_{ij} \tag{50}$$

The extrinsic curvature K_{ij} can also be re-expressed, by splitting it into its trace K and a traceless part $\tilde{A}_{ij}$,

$$\tilde{A}_{ij} = e^{-4\phi}A_{ij} = e^{-4\phi}\left(K_{ij} - \frac{1}{3}K\gamma_{ij}\right) \tag{51}$$

The evolution equation for K can then be found by contracting equation (30) on its indices, giving (bearing in mind equation (39))

$$\partial_t K - \beta^i \partial_i K = -\gamma^{ij} D_i D_j \alpha + \alpha\left(\tilde{A}_{ij}\tilde{A}^{ij} + \frac{1}{3}K^2 + 4\pi(E+S)\right) \tag{52}$$

Subtracting this from equation (30) then gives the evolution of the traceless (or TF, trace-free) part,

$$\begin{aligned}\partial_t \tilde{A}_{ij} - \beta^a \partial_a \tilde{A}_{ij} - \tilde{A}_{ia}\partial_j \beta^a - \tilde{A}_{aj}\partial_i \beta^a = e^{-4\phi}\left(-(D_i D_j \alpha)^{\mathrm{TF}} + \alpha(R_{ij}^{\mathrm{TF}} - 8\pi S_{ij}^{\mathrm{TF}})\right) \\ + \alpha(K\tilde{A}_{ij} - 2\tilde{A}_{il}\tilde{A}^l_j) - \frac{2}{3}\tilde{A}_{ij}\partial_a \beta^a\end{aligned} \tag{53}$$

The same contraction and subtraction on equation (17) gives

$$\partial_t \phi - \beta^i \partial_i \phi = -\frac{1}{6}\alpha K + \frac{1}{6}\partial_i \beta^i \tag{54}$$

and

$$\partial_t \tilde{\gamma}_{ij} - \beta^a \partial_a \tilde{\gamma}_{ij} - \tilde{\gamma}_{ia}\partial_j \beta^a - \tilde{\gamma}_{aj}\partial_i \beta^a = -2\alpha\tilde{A}_{ij} - \frac{2}{3}\tilde{\gamma}_{ij}\partial_a \beta^a \tag{55}$$

The remaining equations of the BSSN formulation are found by decomposing the Ricci tensor R_{ij} into a conformal part, $\tilde{R}_{ij}$, and the rest, R^{ϕ}_{ij}. These can then be given in terms of the conformal connection functions $\tilde{\Gamma}^i = \tilde{\gamma}^{ab}\tilde{\Gamma}^i_{ab}$ and ϕ as

$$R^{\phi}_{ij} = -2(\tilde{D}_i\tilde{D}_j\phi + \tilde{\gamma}_{ij}\tilde{\gamma}^{lm}\tilde{D}_l\tilde{D}_m\phi) + 4((\tilde{D}_i\phi)(\tilde{D}_j\phi) - \tilde{\gamma}_{ij}\tilde{\gamma}^{lm}(\tilde{D}_l\phi)(\tilde{D}_m\phi)) \tag{56}$$

and

$$\tilde{R}_{ij} = -\frac{1}{2}\tilde{\gamma}^{lm}\partial_m\partial_l\tilde{\gamma}_{ij} + \tilde{\gamma}_{k(i}\partial_{j)}\tilde{\Gamma}^k + \tilde{\Gamma}^k\tilde{\Gamma}_{(ij)k} + \tilde{\gamma}^{lm}(2\tilde{\Gamma}^k_{l(i}\tilde{\Gamma}_{j)km} + \tilde{\Gamma}^k_{im}\tilde{\Gamma}_{klj}) \tag{57}$$

with the conformal connection

$$\tilde{\Gamma}^i_{jk} = \frac{1}{2}\tilde{\gamma}^{ia}(\tilde{\gamma}_{aj,i} + \tilde{\gamma}_{ia,j} - \tilde{\gamma}_{ij,a}) \tag{58}$$

The connection functions themselves evolve as

$$\begin{aligned}\partial_t\tilde{\Gamma}^i - \beta^j\partial_j\tilde{\Gamma}^i + \tilde{\Gamma}^j\partial_j\beta^i = & -2\tilde{A}^{ij}\partial_j\alpha + 2\alpha\left(\tilde{\Gamma}^i_{jk}\tilde{A}^{kj} - \frac{2}{3}\tilde{\gamma}^{ij}\partial_j K - 8\pi\tilde{\gamma}^{ij}p_j + 6\tilde{A}^{ij}\partial_j\phi\right) \\ & + \frac{2}{3}\tilde{\Gamma}^i\partial_j\beta^j + \frac{1}{3}\tilde{\gamma}^{li}\partial_l\partial_j\beta^j + \tilde{\gamma}^{lj}\partial_j\partial_l\beta^i\end{aligned} \tag{59}$$

This system of equations can then be shown to be strongly hyperbolic [12].

2.6 Z4 system

An alternative strongly hyperbolic formulation of the Einstein equation is the Z4 system [13]. To obtain these equations, the Einstein equations (29) are modified to include the variables Z_a, as

$$G_{\mu\nu} + \nabla_\mu Z_\nu + \nabla_\nu Z_\mu - \kappa_1[t_\mu Z_\nu + t_\nu Z_\mu - (1+\kappa_2)g_{\mu\nu}t_\sigma Z^\sigma] = 8\pi\left(T_{\mu\nu} - \frac{1}{2}g_{\mu\nu}T\right) \tag{60}$$

where t^μ is a timelike vector field, and can simply be chosen to equal n^μ, the normal vector field to the spacelike hypersurfaces. Z_μ clearly quantifies the deviation from the Einstein equations, and as such it is important that any non-zero components of Z are (at least) damped. This is the case when $\kappa_1 > 0$ and $\kappa_2 > -1$ [13].

While equations (34) and (35) make up four constraint equations on the spacelike hypersurfaces, in the Z4 system these equations are replaced by evolution equations for Z^i and

$\Theta := n_\mu Z^\mu = \alpha Z_0$ (in these coordinates). These equations are given in [13] and [14] as

$$\begin{aligned}(\partial_t - \mathcal{L}_\beta)K_{ij} = &- D_i D_j \alpha + \alpha(R_{ij} + D_i Z_j + D_j Z_i - 2K_i{}^l K_{lj} + (K - 2\Theta)K_{ij} \\ &- \kappa_1(1+\kappa_2)\Theta\gamma_{ij}) - 2\pi\alpha\left(S_{ij} - \frac{1}{2}(S-E)\gamma_{ij}\right)\end{aligned} \tag{61}$$

$$\begin{aligned}(\partial_t - \mathcal{L}_\beta)\Theta = &\frac{\alpha}{2}\left(R + 2\nabla_j Z^j + (K-2\Theta)K - K^{ij}K_{ij} - 2Z^j D_j \ln\alpha\right. \\ &\left. - 2\kappa_1(2+\kappa_2)\Theta - 16\pi E\right)\end{aligned} \tag{62}$$

$$(\partial_t - \mathcal{L}_\beta)Z_i = \alpha\left(\nabla_j(K_i{}^j - \delta_i{}^j K) + \partial_i\Theta - 2K_i{}^j Z_j - \Theta\frac{\alpha_i}{\alpha} - \kappa_1 Z_i - 8\pi p_i\right) \tag{63}$$

together with equation (17). The Lie derivatives have been left in these equations (for brevity), but can be expanded by equation 6 (as they were in the previous sections).

2.7 CCZ4

The GRChombo code uses a system known as CCZ4 (conformal covariant Z4) [14]. This is a combination of the Z4 system in section 2.6 above with a conformal transformation, as in section 2.5. This is seen in the following results[6], where setting $Z^\mu = 0$ returns the BSSN equations of section 2.5 with no modifications. Equations (54) and (55) are unchanged, while equation (53) gains the term

$$e^{-4\phi}\alpha(D_i Z_j + D_j Z_i) - 2\alpha\tilde{A}_{ij}\Theta \tag{64}$$

on the RHS. Similarly, the RHS of equation (52) gains the terms

$$2\alpha(D_i Z^i - K\Theta) - 3\alpha\kappa_1(1+\kappa_2)\Theta \tag{65}$$

Equation (62) is also unchanged, while equation (59) becomes the evolution equation for $\hat{\Gamma}^i := \tilde{\Gamma}^i + 2\tilde{\gamma}^{ij}Z_j$, with $\tilde{\Gamma}^i \to \hat{\Gamma}^i$ and the terms

[6] If comparing these results with the references, it is useful to note that from equation (51), $\tilde{A}_{ij}\tilde{A}^{ij} = K_{ij}K^{ij} - \frac{1}{3}K^2$

$$2\tilde{\gamma}^{ij}\left(\alpha\partial_j\Theta - \Theta\partial_j\alpha - \frac{2}{3}\alpha K Z_j - \alpha\kappa_1 Z_j\right) + 2\kappa_3\left(\frac{2}{3}\tilde{\gamma}^{ij}Z_j\partial_k\beta^k - \tilde{\gamma}^{jk}Z_j\partial_k\beta^i\right) \qquad (66)$$

added to the RHS, including a new damping term controlled by κ_3. Equations (56) and (57) are also unchanged.

Together with the matter evolution equations of section 2.3, this gives the full CCZ4 formulation of General Relativity as equations (54), (55) and (62) as they are, and equations (52), (53) and (59) with the relevant modifications. The dynamical variables that evolve by these equations are (respectively) $\phi, \tilde{\gamma}_{ij}, \Theta, K, \tilde{A}_{ij}$, and $\hat{\Gamma}^i$. Equations (56) and (57) then give the Ricci tensor in this scheme.

2.8 Choices of foliation

Up until this point, no specific choice has been made for the lapse α or the shift β^i. These four degrees of freedom represent the general (diffeomorphism) covariance of general relativity, i.e., the invariance of the field equations under coordinate transformations. In this section, various possible choices will be explored, and their benefits/drawbacks will be described and compared.

The most obvious choice for the lapse and shift is known as geodesic slicing, and is given by setting $\alpha = 1$ and $\beta^i = 0$ everywhere. It is instructive to consider the perspectives of 'coordinate observers' in these various schemes, who move with velocities v^μ equal to the vector ∂_t, which corresponds to the infinitesimal dispacement vector dl between points with the same spacial coordinates on neighbouring slices. Clearly, in this case, their velocity is equal to n^μ (which is also equal to m^μ since $\alpha = 1$), which also makes them 'normal observers'.

It turns out that these observers have vanishing acceleration, and therefore correspond to geodesics. While this may also seem usefully simple, it poses a significant problem if these coordinate choices are used in numerial simulations — since geodesics often converge to coordinate singularities in finite proper time (e.g., falling 'into' a black hole singularity), these coordinates correspondingly become singular.

An alternative choice that avoids this issue is known as maximal slicing. By requiring

that the mean curvature $K = 0$, and that normal observers neither converge nor diverge, it can be shown that the lapse α must obey the condition,

$$D^2\alpha = \alpha(K_{ij}K^{ij} + 4\pi(E + S)) \tag{67}$$

The name 'maximal slicing' illustrates the fact that this choice maximises the volume of spacial foliations, as shown in section 10.2.2 of [8].

A common category of conditions for the lapse is known as harmonic slicing [15], where the time coordinate is required to obey $\nabla_\mu \nabla^\mu t = 0$. This gives the following condition on the lapse,

$$(\partial_t - \mathcal{L}_\beta)\alpha = -K\alpha^2 \tag{68}$$

Following the work in [16], generalising the RHS of equation (68) to $-K\alpha^2 f(\alpha)$ encapsulates both this harmonic slicing condition ($f(\alpha) = 1$) and the geodesic slicing condition ($f(\alpha) = 0$). Taking $f(\alpha) = \frac{2}{\alpha}$ gives the very common '1+log' slicing, so named for a solution to this condition with vanishing shift; $\alpha = 1 + \ln\gamma$. This choice is particularly useful for avoiding these coordinate singularities, and as a result it is regularly chosen in numerical simulations.

A popular combination of conditions is this 1+log condition for α with the 'hyperbolic gamma-driver' condition for the shift β,

$$\partial_t^2 \beta^i = k\partial_t \hat{\Gamma}^i - (\eta - \partial_t \ln k)\partial_t \beta^i \tag{69}$$

where the $\hat{\Gamma}^i$ were defined in section 2.7, and both $k, \eta > 0$. This is equivalent to the following pair of first-order PDEs,

$$\partial^t \beta = kB^i \tag{70}$$

$$\partial_t B^i = \partial_t \hat{\Gamma}^i - \eta B^i \tag{71}$$

This combination of conditions is known as the moving-punctures method [17].

3 Flavour Oscillations

Reference has already been made to the particle and field pictures of flavour oscillations. In the particle picture, the primary objects of interest are small test masses, travelling along (approximately) null geodesics and picking up a phase change along these paths. The oscillation probability for a 2-flavour particle travelling along these geodesics can then be found by comparing the phases of the two mass eigenstates. In the field picture, the flavour fields are evolved indirectly as a doublet of massive complex scalar fields, which are then rotated back to the flavour basis at each point to give the probability of oscillation there. In this section, both pictures will be used. First, an expressions will be found (in the field picture) for the oscillation probability of a plane wave travelling though flat space. Then, an expression will be obtained through the particle picture for the phase change along geodesics in the Kerr spacetime. This result can then be compared to the field picture by considering an infinite plane of particles coming in from infinity and scattering past the black hole. This comparison to the field picture will allow for the equations derived here to guide the numerical investigations of both this work and future research.

3.1 Flat space

A particle is considered with two flavour eigenstates, labelled a and b. The two mass eigenstates, labelled $+$ and $-$, do not correspond directly to the two flavour eigenstates, and are instead related by the mixing matrix,

$$\begin{pmatrix} \phi_+ \\ \phi_- \end{pmatrix} = \begin{pmatrix} \cos(\alpha) & \sin(\alpha) \\ -\sin(\alpha) & \cos(\alpha) \end{pmatrix} \begin{pmatrix} \phi_a \\ \phi_b \end{pmatrix} \tag{72}$$

which is clearly just a regular U(1) rotation.

As the mass eigenstates obey the Klein-Gordon equation (equation 40), the probability of a plane-wave state $|A\rangle$ evolving into a state $|B\rangle$ at position $\vec{r}_j$ in a time t is given by

$$P_{A\to B} = |\langle B|U_A(t,\vec{r})|A\rangle|^2, \tag{73}$$

where $U_A(t,\vec{r})$ is the evolution operator for state A, given in the $|\pm\rangle$ basis by,

$$U_A(t,\vec{r}) = \begin{pmatrix} e^{i(-\omega_+ t+\vec{k}\cdot\vec{r})} & 0 \\ 0 & e^{i(-\omega_- t+\vec{k}\cdot\vec{r})} \end{pmatrix} \tag{74}$$

where w_A is the energy of some state $|A\rangle$, and $\vec{k}$ is its momentum. As usual, w_A and $\vec{k}$ obey the energy-momentum relationship $w_A^2 = |\vec{k}|^2 + m_A^2$, where m_A is the mass of state $|A\rangle$. It has already been assumed implicitly that the momenta of the two mass eigenstates are equal, an assumption that is justified if they are highly relativistic and produced by the same source. If state $|A\rangle$ corresponds to flavour a and state $|B\rangle$ corresponds to flavour b, this probability is given simply by,

$$P_{A\to B} = \sin^2(2\alpha)\sin^2\left(\frac{w_+ - w_-}{2}t\right). \tag{75}$$

3.2 Curved space

3.2.1 Non-radial escape from black hole region

In the particle picture, the expression for the phase change of each mass eigenstate travelling along a geodesic $\mathcal{C}$ is found from the exponenents in equation (74), which can be suggestively written as,

$$\phi = \int_{\mathcal{C}} p_\mu dx^\mu \tag{76}$$

In the flat space case, this reduces simply to $-\omega_+ t + \vec{k}\cdot\vec{r}$, but in a gravitational field it is more complicated to analyse. As in [2], this can be analytically evaluated for geodesics in the Schwarzschild metric when some approximations are made.

In this work, the result in [2] will be extended from the Schwarzschild case to include black holes with spin. However, for the analytic approximation, it will be assumed that both a and M are small (i.e., low angular momentum per unit mass and low total mass) compared to r along the geodesics followed by the neutrinos. Once the paths have been integrated, it will then be assumed that the beginning and end points are far from the black hole, specifically in comparison to the impact parameter. This limits the applicability of the

resulting equations to regions far from the black hole, but the full (strong gravity, high rotation) case will be evaluated numerically in later sections.

It has been shown in [18] that in Kerr spacetimes, unlike Schwarzschild, the effect of spin-flip on flavour oscillations is important. This occurs because neutrino-like particles should, in principle, be modelled by spinor fields, with a non-trivial interaction between their intrinsic angular momentum and the angular momentum of the black hole. However, as shown in [18], the conditions under which this effect is important are very restrictive in cases of low a, and therefore this effect is not considered here. With these approximations, the Kerr metric in Boyer–Lindquist coordinates is simplified to

$$g_{\mu\nu} \approx \begin{pmatrix} -B(r) & 0 & 0 & \frac{-4Ma\ \sin^2(\theta)}{r} \\ 0 & B(r)^{-1} & 0 & 0 \\ 0 & 0 & r^2 & 0 \\ \frac{-4Ma\ \sin^2(\theta)}{r} & 0 & 0 & r^2 sin^2(\theta) \end{pmatrix} \tag{77}$$

where $B(r) = 1 - \frac{2M}{R}$.

The (approximate) inverse metric, which will be needed later, is also given as,

$$g^{\mu\nu} = \begin{pmatrix} \frac{r^2 \sin^2(\theta)}{|g_{red}|} & 0 & 0 & \frac{4Ma\ \sin^2(\theta)}{r|g_{red}|} \\ 0 & B(r) & 0 & 0 \\ 0 & 0 & r^{-2} & 0 \\ \frac{4Ma\ \sin^2(\theta)}{r|g_{red}|} & 0 & 0 & \frac{-B(r)}{|g_{red}|} \end{pmatrix} \approx \begin{pmatrix} -B(r)^{-1} & 0 & 0 & \frac{-4Ma}{r^3 B(r)} \\ 0 & B(r) & 0 & 0 \\ 0 & 0 & r^{-2} & 0 \\ \frac{-4Ma}{r^3 B(r)} & 0 & 0 & \frac{1}{r^2 \sin^2(\theta)} \end{pmatrix} \tag{78}$$

where $|g_{red}|$ in the first term is the modulus of the reduced matrix (which excludes the middle four values),

$$|g_{red}| = r^2 \left(-B(r) \sin^2(\theta) - \frac{16M^2 a^2 \sin^2(\theta)}{r^4} \right) \tag{79}$$

However, the second term in equation (79) is of order $(\frac{a^2}{r^4})$ and so has been dropped.

Since highly relativistic neutrinos are assumed, the path $\mathcal{C}$ will be taken along null geodesics. It will also be assumed from here on that θ is fixed at $\frac{\pi}{2}$, so $d\theta = 0$. The path

will be parameterised by the r coordinate, and the following quantities will be needed,

$$E_0 \equiv g_{t\nu}\frac{dx^\nu}{ds},\ J_0 \equiv g_{\phi\nu}\frac{dx^\nu}{ds},\ p_0(r) \equiv g_{r\nu}\frac{dx^\nu}{ds} \tag{80}$$

From the absence of t and ϕ in the metric, it is clear that dt and $d\phi$ are Killing vector fields. As a result, the quantities E_0 and J_0 are conserved along these geodesics.

From this set of coupled equations, the following differentials are found on the null geodesics, as needed to express dx^μ as $\frac{dx^\mu}{dr}dr$,

$$\left(\frac{dr}{ds}\right)_0 = B(r)p_0(r) \tag{81}$$

$$\left(\frac{d\phi}{ds}\right)_0 = \frac{\frac{J_0 r}{4Ma} - \frac{E_0}{B(r)}}{\frac{4Ma}{rB(r)} + \frac{r^3}{4Ma}} \approx \frac{1}{r^2}\left(J_0 - \frac{4MaE_0}{rB(r)}\right) \tag{82}$$

$$\left(\frac{dt}{ds}\right)_0 = -\frac{E_0}{B(r)} - \frac{4Ma}{rB(r)}\frac{d\phi}{ds} \approx -\frac{E_0}{B(r)} - \frac{4MaJ_0}{r^3} \tag{83}$$

where the subscript '$_0$' refers to the null geodesic.

These quantities are also related by the condition,

$$g^{\mu\nu}p_\mu p_\nu = 0, \tag{84}$$

allowing for the quantity $p_0(r)$ to be given in terms of the conserved quantities E_0 and J_0 as,

$$B(r)p_0(r) = E_0\sqrt{1 - \frac{B(r)b^2}{r^2} + \frac{8Mab}{r^3}} \tag{85}$$

where the relation $J_0 = E_0 b$ has been used, defining b as the *impact parameter*.

Similarly, defining

$$p_\mu^{(k)} = m_k g_{\mu\nu}\frac{dx^\nu}{ds} \tag{86}$$

gives the conserved quantities $E_k \equiv p_t^{(k)}$ and $J_k \equiv p_t^{(k)}$, and the constrained quantity $p_k(r) \equiv p_r^{(k)}$ (with J_k and $p_k(r)$ therefore the negative of those in [2]).

The constraint for $p_k(r)$ contains the mass,

$$g^{\mu\nu} p_\mu^{(k)} p_\nu^{(k)} = m_k^2 \tag{87}$$

giving the approximate expression,

$$B(r) p_k(r) \approx E_k \sqrt{1 - \frac{B(r) b^2}{r^2} + \frac{8Mab}{r^3}} \left[1 - \frac{m_k^2 B(r)(1 - b^2/r^2)}{2E_k^2 (1 + 8Mab/r^3 - B(r) b^2/r^2} \right] \tag{88}$$

where the assumption of relativistic particles allows for an expansion in $\frac{m_k^2}{E_k^2}$. The full expression for the phase,

$$\Phi_k = \int_{r_A}^{r_B} \left[E_k \left(\frac{dt}{dr} \right)_0 + p_k(r) + J_k \left(\frac{d\phi}{dr} \right)_0 \right] dr \tag{89}$$

can now be evaluated, using equations (81) to (83) for the differentials in (89),

$$\left(\frac{dt}{dr} \right)_0 = \frac{1}{B(r) p_0(r)} \left(\frac{dt}{ds} \right)_0 \tag{90}$$

$$\left(\frac{d\phi}{dr} \right)_0 = \frac{1}{B(r) p_0(r)} \left(\frac{d\phi}{ds} \right)_0 \tag{91}$$

and finding,

$$\Phi_k = \int_{r_A}^{r_B} \frac{E_0}{B(r) p_0(r)} \left[-\frac{E_k}{B(r)} - \frac{4MabE_k}{r^3} + \frac{B(r) p_o(r)}{E_0} p_k(r) + J_k \left(\frac{b}{r^2} - \frac{4Ma}{r^3 B(r)} \right) \right] dr \tag{92}$$

Then, using equations (85) and (88),

$$B(r) p_0(r) p_k(r) = \frac{E_0 E_k}{B(r)} \left(1 + \frac{8Mab}{r^3} - \frac{B(r) b^2}{r^2} - \frac{m_k^2 B(r)}{2E_k^2} \left(1 - \frac{b^2}{r^2} \right) \right) \tag{93}$$

By substituting in for J_k with the velocity at infinity, where the metric is approximately Minkowski,

$$J_k \approx E_k b \left(1 - \frac{m_k^2}{2E_k^2} \right) \tag{94}$$

and employing the weak-field limit, $\frac{M}{r} << 1$, the phase becomes (after lots of cancellation),

$$\Phi_k = \int_{r_A}^{r_B} \frac{E_0 E_k}{B(r)p_0(r)} \left[-\frac{m_k^2}{2E_k^2} + \frac{2Mabm_k^2}{E_k^2 r^3} \right] dr \tag{95}$$

The numerator $B(r)p_0(r)$, given in equation (85), can now be expanded as,

$$\frac{1}{B(r)p_0(r)} \approx \frac{1}{E_0\sqrt{1-\frac{b^2}{r^2}}} \left(1 - \frac{Mb(4a+b)}{r(r^2-b^2)} \right) \tag{96}$$

With this, breaking up the phase in equation (95) gives the following terms,

$$\Phi_k^1 = -\frac{m_k^2}{2E_0} \int_{r_A}^{r_B} \frac{r}{\sqrt{r^2-b^2}} \tag{97}$$

$$\Phi_k^2 = \frac{m_k^2}{2E_0} \int_{r_A}^{r_B} \frac{Mb(4a+b)}{(r^2-b^2)^{3/2}} \tag{98}$$

$$\Phi_k^3 = \frac{2Mabm_k^2}{E_0} \int_{r_A}^{r_B} \frac{1}{r^2\sqrt{r^2-b^2}} \tag{99}$$

and a term of order $\frac{M^2}{r^2}$ that can be discarded.

The integrals in equations (97) to (99) all have known solutions, giving the integrated phase as,

$$\Phi_k \approx \left[-\frac{m_k^2}{2E_0} \left(\sqrt{r^2-b^2} + \frac{M(4a+b)r}{b\sqrt{r^2-b^2}} \right) + \frac{2Mam_k^2}{E_0} \frac{\sqrt{r^2-b^2}}{br} \right]_{r_A}^{r_B} \tag{100}$$

This expression is valid for neutrinos generated in the vicinity of a Kerr black hole, escaping outwards non-radially.

3.2.2 Scattering by black holes

To evaluate the phase for null geodesics passing by the black hole (see figure 4), the phase can be separated into two terms, either side of the point of closest approach r_0,

$$\phi = \int_{r_0}^{r_A} p_\mu dx^\mu + \int_{r_0}^{r_B} p_\mu dx^\mu \tag{101}$$

The value of r_0 can be found by requiring that $\frac{dr}{ds}\big|_{r_0} = 0$. This corresponds to the condition,

$$1 + \frac{8Mab}{r_0^3} - B(r_0)\frac{b^2}{r_0^2} = 0 \tag{102}$$

In the weak field limit, this gives (by solving to a first approximation, then substituting back in),

$$r_0 \approx b\left(1 - \frac{M}{b}\left(\frac{4a}{b} + 1\right)\right) \tag{103}$$

However, the expansion in equation (96) no longer works in this case, as the path contains a region where $r < b$. This not only leads to a negative square root (which could be dealt with by separating the integral around $r = b$ and including an i where necessary), but also leads to the integral going over the divergent point $r = b$. This problem is not described in [2], where only the previous derivation is provided, but can be accounted for by rewriting equation (96) as,

$$\begin{aligned}
\frac{1}{B(r)p_0(r)} &\approx \frac{r}{E_0\sqrt{r^2 - r_0^2}}\sqrt{1 + \left(r_0^2 - b^2 + \frac{2Mb(b+4a)}{r}\right)\frac{1}{r^2 - r_0^2}} \\
&\approx \frac{r}{E_0\sqrt{r^2 - r_0^2}}\left[1 - \frac{1}{2}\left(r_0^2 - b^2 + \frac{2Mb(b+4a)}{r}\right)\frac{1}{r^2 - r_0^2}\right] \\
&= \frac{r}{E_0\sqrt{r^2 - r_0^2}}\left(1 + \frac{M(4a+b)}{r^2 - r_0^2} - \frac{Mb(4a+b)}{r(r^2 - r_0^2)}\right)
\end{aligned} \tag{104}$$

using equation (103) and the weak field condition to approximate

$$r_0^2 - b^2 \approx -2M(4a + b) \tag{105}$$

This gives new terms in the expression for the phase,

$$\Phi_k^1 = -\frac{m_k^2}{2E_0}\int_{r_A}^{r_B}\frac{r}{\sqrt{r^2-r_0^2}} \tag{106}$$

$$\Phi_k^2 = \frac{Mb(4a+b)m_k^2}{2E_0}\int_{r_A}^{r_B}\frac{1}{(r^2-r_0^2)^{3/2}} \tag{107}$$

$$\Phi_k^3 = \frac{2Mabm_k^2}{E_0}\int_{r_A}^{r_B}\frac{1}{r^2\sqrt{r^2-r_0^2}} \tag{108}$$

$$\Phi_k^4 = \frac{-M(4a+b)m_k^2}{2E_0}\int_{r_A}^{r_B}\frac{r}{(r^2-r_0^2)^{3/2}} \tag{109}$$

This gives the phase again as,

$$\Phi_k \approx \left[-\frac{m_k^2}{2E_0}\left(\sqrt{r^2-r_0^2}+\frac{M(4a+b)br}{r_0^2\sqrt{r^2-r_0^2}}-\frac{M(4a+b)}{\sqrt{r^2-r_0^2}}\right)+\frac{2Mam_k^2}{E_0}\frac{\sqrt{r^2-r_0^2}}{br}\right]_{r_0}^{r_A}+\Big[...\Big]_{r_0}^{r_B} \tag{110}$$

which, using that $r_0 \approx b$ at first order, can be written out as,

$$\Phi_k \approx \left[-\frac{m_k^2}{2E_0}\left(\sqrt{r^2-r_0^2}+\frac{M(4a+b)}{b}\sqrt{\frac{r-r_0}{r+r_0}}\right)+\frac{2Mam_k^2}{E_0}\frac{\sqrt{r^2-r_0^2}}{br}\right]_{r_0}^{r_A}+\Big[...\Big]_{r_0}^{r_B} \tag{111}$$

Each of the resulting terms can then be expanded out as follows,

$$\sqrt{r_{A/B}^2-r_0^2} \approx r_{A/B}-\frac{b^2}{2r_{A/B}}+\frac{M(4a+b)}{r_{A/B}} \tag{112}$$

$$\frac{M(4a+b)}{b}\sqrt{\frac{r_{A/B}-r_0}{r_{A/B}+r_0}} \approx \frac{M(4a+b)}{b}\left(1-\frac{b}{r_{A/B}}\right) \tag{113}$$

$$\frac{2Mam_k^2}{E_0b}\frac{\sqrt{r^2-r_0^2}}{r} \approx \frac{2Mam_k^2}{E_0b} \tag{114}$$

Bringing these together gives the fully integrated phase as,

$$\Phi_k = -\frac{m_k^2}{2E_0}\left(r_A+r_B-\frac{b^2}{2r_a}-\frac{b^2}{2r_B}+\frac{2M(4a+b)}{b}\right)+\frac{4Mam_k^2}{E_0b} \tag{115}$$

The two terms containing a cancel out, and rearranging gives the same expression found for the Schwarzschild case in [2],

$$\Phi_k = -\frac{m_k^2}{2E_0}(r_A + r_B)\left(1 - \frac{b^2}{2r_A r_B} + \frac{2M}{(r_A + r_B)}\right) \tag{116}$$

In [1], this final result (which is considered there for just the Schwarzschild case) has been used to find the equivalent expression to equation (75) for a plane wave of particles, scattered by a non-rotating black hole. The phase difference at a point beyond the black hole is then affected by both the phase difference of two mass eigenstates travelling along each geodesic, and the interference of two *different* geodesics meeting there. The coordinates of each point beyond the black hole are related to the impact parameters of the two null geodesics (coming in from infinity) that intersect there, and these impact parameters then allow for the phase difference to be calculated (using equation (116)) at the intersection point. Using this phase difference then gives an expression for the oscillation probability,

$$\begin{aligned} P_\infty = \sin^2(2\alpha)\Bigg[&\sin^2\left(\frac{\Delta m^2}{4k}\left(r - \frac{\Sigma b^2}{4r}\right)\right)\cos\left(\frac{m_+^2\Delta b^2}{8kr}\right)\cos\left(\frac{m_-^2\Delta b^2}{8kr}\right) \\ &+ \sin^2\left(\frac{\Sigma m^2 \Delta b^2}{16kr}\right)\sin^2\left(\frac{\Delta m^2 \Delta b^2}{16kr}\right)\Bigg] \end{aligned} \tag{117}$$

where for any variable v, $\Delta v^2 = v_1^2 - v_2^2$ and $\Sigma v^2 = v_1^2 + v_2^2$. The two impact parameters b_1 and b_2 correspond to the impact parameters of the two geodesics meeting at the given point, m_+ and m_- correspond to the mass eigenstate masses, and k corresponds to their (roughly equal) momenta. Figure 4 shows two example geodesics, with the impact parameters and points of closest approach displayed.

3.3 Conclusions from analytic expressions

Before going on to consider the full numerical simulation of this scenario, it it useful to consider what has been found, and what is to be expected from the results in this section. The first equation to consider is equation (75), which gives the probability of oscillation in flat space. While the flat space scenario is not directly of interest here, it is known that

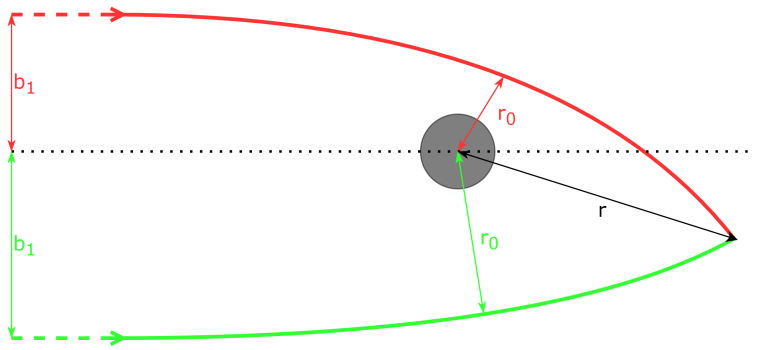

Figure 4: A depiction of two geodesics with impact parameters b_1 and b_2, meeting at a point with radial coordinate r (in Boyer-Lindquist coordinates centred on the black hole). The points of closest approach r_0 are also included, with red and green corresponding to the two different geodesics.

both the Schwarzschild and the Kerr geometries are asymptotically flat [19]. This means that equation (75) can be used to predict the probability oscillation length far from the black hole. Assuming relativistic particles (so $\Delta t \approx \Delta L$ along their paths), the oscillation length is given by

$$L \approx \frac{2\pi}{\omega_1 - \omega_2} = \frac{2\pi}{\sqrt{k^2 + m_1^2} - \sqrt{k^2 + m_2^2}} \tag{118}$$

This can serve as a simple check for the validity of the simulations in section 5.

Equation (100) with $a \to 0$ clearly becomes equation (55) in [2], implying that this expression is valid for particles created in the vicinity of a black hole and escaping outwards non-radially. However, as discussed in section 3.2.2, this expression is not valid for neutrinos passing by a black hole. In this case, equations (111) and (116) are valid, and again taking $a \to 0$ reduces these to equations (58) and (59) in [2]. The derivation here also serves as a derivation for the results in [2], where they are not proved in the case of scattering.

As mentioned in the section 1, one of the most interesting features of this phenomenon is its relation to the absolute particle masses (rather that just their difference). Equation (117) makes manifest this connection. The oscillation pattern is clearly dependent on both the sum of the squared masses and their difference. This means that by observing the oscillation pattern, one could (in principle) deduce the masses of these two fields.

4 Numerical Methods

In this work, the GRChombo numerical relativity code has been used — much of the information presented here can be found (in more detail) in reference [10].

The fundamental 'object' in the numerical simulation is a grid of points, discretised in both space and time. The 3+1 formulation of section 2.2 allows for the full 4-dimensional spacetime to be modelled as a 3-dimensional space that is evolved in the time direction, based on the evolution equations. As described in section 2.2, there are many possible formulations of General Relativity that could be used for this method. Here, the CCZ4 formulation has been used, with the gauge conditions set by the choice of Kerr-Schild coordinates [20].

In the simulations presented in section 5, a fixed background has been used (i.e., no backreaction on the metric). This means that most of the numerical capabilities of the GRChombo code have not been used. However, the full workings of the GRChombo code will be outlined in this section, as they will be needed for the future investigations described earlier and in section 6.

4.1 Runge-Kutta 4

The standard technique for evolving first-order time differentials of the form $\partial_t v = f(v)$ is known as 4th-order Runge-Kutta, or RK4 (see section 2.8 of [21] for details). This algorithm allows for an accurate approximation of the value $v|_{t+\delta t}$, provided that v and its derivatives are known at time t, with a global error of order $O(\Delta t^4)$. This means that the error across many steps of length Δt reduces quartically with a reduction in Δt.

In this case, the evolution is of the CCZ4 equations in section 2.7. To find the necessary differentials of the dynamical variables listed in section 2.7, the stencils of equations (2.2) to (2.6) of [22] are used. These stencils require that, for the derivative of f along the e_i direction, the values of f at the points p, $p \pm he_i$, and $p \pm 2he_i$ are known, where h is the spacing between grid points. This then gives approximations of these spatial derivatives with an error that is order $O(h^4)$ in the grid spacing.

4.2 Adaptive mesh refinement

While the finite-difference method described above is fairly robust, the use of these schemes for a large uniform grid in 3 dimensions would be extremely computationally expensive. This is particularly important where the function f varies significantly over some small area of its domain (as the variables of GR simulations do near black holes), since this would require a finer grid over the whole domain. In d spatial dimensions, the computational cost clearly goes as $1/h^d$.

The solution to this problem used in GRChombo is called AMR (Adaptive Mesh Refinement), which, as described in [23], involves two main steps; the flagging of regions with insufficient resolution, and the regridding of these regions.

For each regridding, the cells in the grid are tagged according to the variation of selected fields ϕ across each cell. If the norm of the variation of these fields across a cell is greater than some chosen value $\sigma(\phi)$, the cell is tagged for regridding.

$$\text{Tagged} = \begin{cases} \text{True } (1) & \text{for} \quad |\Delta\phi| > \sigma(\phi) \\ \text{False } (0) & \text{otherwise} \end{cases} \tag{119}$$

where in d dimensions,

$$|\Delta\phi(p)| = \sqrt{\sum_{i=1}^{d} (\phi(\boldsymbol{p} + h\boldsymbol{e_i}) - \phi(\boldsymbol{p} - h\boldsymbol{e_i}))^2} \tag{120}$$

Once the cells have been tagged, the grid must be partitioned for regridding. The primary goal of this partitioning procedure is to maximise the efficiency, i.e., the ratio of tagged to total cells in the regions that are to be regridded. GRChombo uses block-structured AMR, where the partitioned regions are rectangular (in cell coordinates). Clearly, regridding into smaller regions increases the efficiency.

However, since the different regions are (in general) handled by different processors, dividing into a large number of regions may be less computationally efficient when load-balancing (the distribution of work between processors) is considered, and with the need

for ghost cells along boundaries to exchange information between processors.[7]

To regrid a particular region, the first step is to look for 'holes', where the plane Π_{p_i}, perpendicular to the direction given by e_i at the point p_i, contains only untagged cells. Boundaries are first drawn along these lines. To draw a boundary across a direction with no holes, each coordinate x_i is first associated with the (technically discrete) functions,

$$X_i(x_i) = \sum_{p \in \Pi_{p_i}} \text{Tagged}|_p \tag{121}$$

and the Laplacians $\partial^2_{x_i} X_i$. The zero crossings of these Laplacians can then be used to identify the inflection points in the functions X_i, which correspond to local extrema in the rate of change of X_i. This makes intuitive sense, since a grid like that in figure 5 would be divided along the obvious choice, the red line, which corresponds to one of these zero crossings. If there are multiple inflection points, the one with the largest change in $\partial^2_{x_i} X_i$ is selected, as this corresponds to the narrowest peak in $\partial_{x_i} X_i$, i.e., the sharpest change in the gradient of tagged-cell density.

The efficiency $\epsilon = \dfrac{\text{tagged cells}}{\text{total cells}}$ is then compared to a pre-defined 'fill-factor', and if it is higher than this the partitioning of that box is stopped. If not, it is partitioned further until either all boxes satisfy the fill-factor condition, or further partitioning is impossible. The grid within each partitioned box containing tagged cells is then refined by a chosen ratio, and the whole process is repeated until no unrefined cells pass the tagging criterion of equation (120).

4.3 Instabilities and Kreiss-Oliger dissipation

In practice, finite difference schemes used in numerical simulations are very prone to instabilities. This renders many schemes, that in theory should approximate the true evolution of a system, useless. Numerical errors may, for example, be caused by spurious reflections at the boundaries, or along regridding lines. In unstable schemes these errors are then propagated forwards in time, or even amplified exponentially. Provided that the

[7] As mentioned in [23], the inclusion of vectorisation in one particular direction also skews the ideal regridding procedure.

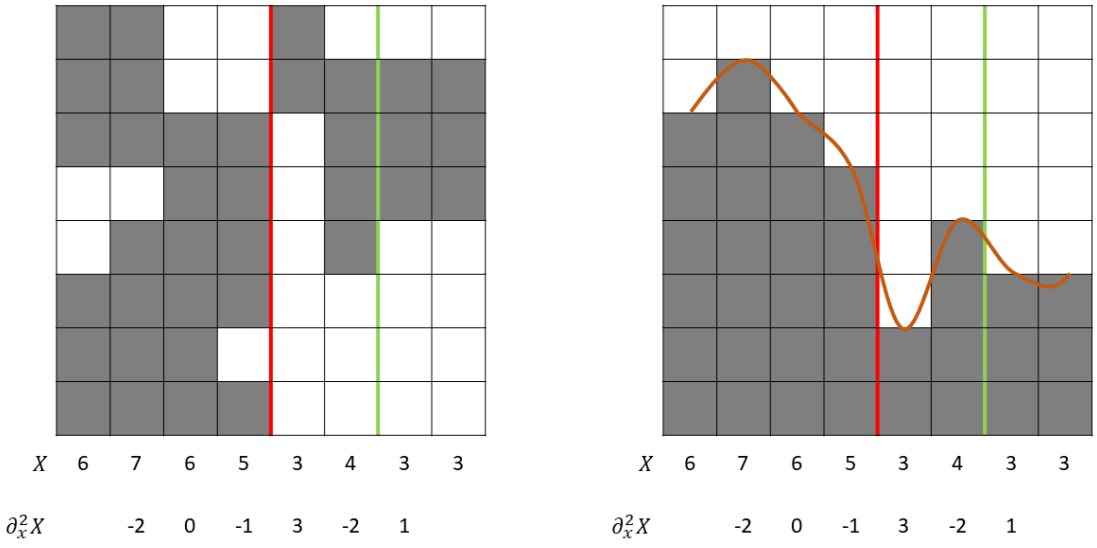

Figure 5: The left hand side shows an example grid, with values of X and $\partial^2_{x_i} X_i$ shown (X running from left to right, tagged cells in grey). The red and green lines show zero crossings of $\partial^2_{x_i} X_i$, with the red line chosen as the boundary due the largest change in $\partial^2_{x_i} X_i$.
The right hand side shows the same grid but 'stacked', with a curve drawn on top to show the inflection points more clearly.

evolution scheme is conditionally stable (i.e., stable for small enough Δt), many causes of numerical error can be solved by simply increasing the resolution. However, as mentioned previously, this is computationally very expensive in higher dimensional systems.

There are many alternative methods for dealing with these errors. Many spurious field excitations occur in very high frequency modes, and these can be damped out by the introduction of a dissipative term. This term corresponds to the addition of a diffusive term in the original equation, which goes to zero as $\frac{\Delta t}{\Delta x} \to 0$. In GRChombo, 3rd order Kreiss-Oliger dissipation is used, as described in [24]. While this artificial dissipation may appear to affect the physics, it only affects higher frequency modes. These modes are not captured well at lower resolutions and therefore should not be trusted regardless.

4.4 Boundary conditions

The simplest and safest way to avoid issues at the boundaries of the simulation is to keep them out of causal contact with the system being studied. However, certain choices of boundary conditions may be preferable, not least for the sake of reducing the area needing simulation.

As mentioned previously, ghost cells exist at all boundaries (internal boundaries as well as the outer boundaries of the simulation). These cells are needed for the 4th-order stencils at points on the boundaries. The choice of boundary conditions dictates how the outer ghost cells should be filled, enforcing the desired conditions along the boundary.

Common choices include periodic, fixed, extrapolating, Sommerfeld, and reflective boundary conditions. Periodic conditions are useful where the simulation's domain can be considered as a small part of a large, repeating (periodic) system. The values of the ghost cells on one side are then filled by the values of the cells on the opposite side — this requires that the domain is large enough for no feature to directly interact with itself. Fixed/Dirichlet boundary conditions enforce some predetermined values of the relevant variables along the boundary. Extrapolating boundary conditions may be implemented up to (in principle) any order, where the outermost layers of cells are used to predict the form of each extrapolating variable for the ghost cells outside the boundary. Reflective boundary conditions are used for variables with a clear symmetry in one direction, and fills the ghost cells with a reflection of the cells inside the boundary (with the parity of these variables also accounted for). This gives stencils near and along the boundary that are indistinguishable from idealised systems with perfect symmetry that are simulated over twice the domain. As a result, these boundary conditions are frequently used (as they are in this work) to reduce the computational cost of highly symmetric simulations.

Sommerfeld boundary conditions enforce the dissipation of outgoing radiation. For a field ϕ with Sommerfeld boundaries, the condition

$$\partial_t \phi = -\frac{v x_i}{r} \partial_i \phi - v \frac{\phi - \phi_0}{r} \tag{122}$$

is enforced at the boundaries, where r is the radius and ϕ_0 is the desired value 'at infinity'.

5 Simulations of Neutrino Oscillations

5.1 Geometrized units

It is common in physics to choose systems of units based on the fundamental constants of nature; such units are described as 'natural'. In this work, geometrized units are used. This is often described as 'setting' the speed of light c and the gravitational constant G to 1. While true, the meaning of this statement (particularly dimensionally) is often unclear, so an alternate (but entirely equivalent) interpretation will be given here.

In the standard SI system of units, these constants have units of $[\mathrm{ms}^{-1}]$ and $[\mathrm{m}^3\mathrm{kg}^{-1}\mathrm{s}^{-2}]$ respectively. This system of units leaves factors of c and G in many equations. To remove these factors, it is useful to equate certain units. For example, if it is chosen that 3×10^8 metres will be considered equivalent to 1 second, the speed of light becomes 1 second per second, or 1 metre per metre — i.e., just 1. This fixes the relationship between units of time and length, and must be remembered when amounts of time (now measured in metres) are desired in seconds[8]. Velocities, such as the speed of light itself, can now be considered dimensionless in these units. This reparametrisation of time (or equivalently of length) also affects the relative dimensions of other physical quantities. For example, take the energy-momentum relation; $E^2 = m^2c^4 + p^2c^2$. In SI units, c is required here to relate the different dimensions of energy, mass, and momentum. In geometric units, where velocities are now dimensionless, the dimensions of mass, energy and momentum must clearly be the same.

In a similar spirit, the constant G can be removed from equations by equating one kilogram with $\frac{G}{c^2}$ metres (where c and G are just the numerical values of these constants in SI units). This then fixes the relationship of mass to both length and (via length) to time[9].

To recover the dimensions of length, time, and mass, units of length must be converted into their 'equivalent' quantities in these units. Table 1 shows some useful conversions between quantities in SI units and geometrized units.

[8]This makes intuitive sense in the context of general relativity, where length and time are considered to be truly equivalent. The constant c can then be considered an artifact of an obfuscating system of units. Alternatively, this can all be considered as just a useful tool for decluttering equations.

[9]In particle physics literature, the reduced Planck constant $\hbar$ is often set to one, rather than the gravitational constant G. This causes energy and mass to have dimensions of *inverse* length (/time).

Dimensions and conversions			
Quantity	Standard dimension	Geometrized dimension	Conversion factor
Length	$[L]$	$[L]$	1
Time	$[T]$	$[L]$	c
Velocity	$[LT^{-1}]$	1	c^{-1}
Mass	$[M]$	$[L]$	Gc^{-2}
Energy	$[LT^{-2}M]$	$[L]$	Gc^{-4}
Angular Momentum	$[L^2T^{-1}M]$	$[L^2]$	Gc^{-3}

Table 1: The dimensions of various quantities in standard (SI) units and geometrized units. To convert from the latter into the former, a given quantity should be multiplied by the factor in the rightmost column (e.g., 1 [second] = c [metres]).

An equation written in geometrized units can be converted into SI units by multiplying each quantity with its conversion factor. These conversion factors are then dimensionful, as required for consistency.

Most values given for the simulations in this section will be given in terms of geometrized length units. The scale of these units is not fixed, so they be chosen to represent any length. A useful scale comes from setting the black hole mass equal to 0.5 [L], so that each unit of length corresponds to one Schwarzschild radius ($R_S = 2M$ in geometrized units). For a solar mass black hole, the Schwarzschild radius is roughly 1.5km. However, the particle masses are the exception. These will be given in units of inverse length, such that 1 [particle mass unit] = $\frac{1}{\lambda_C}$, where λ_C is the Compton wavelength corresponding to the particle mass. With length scales measured in Schwarzschild radii and a solar mass black hole, this means that masses of 1 correspond to $\sim 4 \times 10^{-10}$eV. This conversion can be done more generally by $m[J] = \frac{hc^3 M_P}{2GM_B}$, where $m[J]$ is the mass in Joules, M_P is the particle mass in inverse Schwarzschild radii, and M_B is the black hole mass in kg.

5.2 Simulated physical system

The physical system under investigation is essentially the same as that in section 3. However, while the viewpoint of that section was of a 2-dimensional 'sheet' of particles travelling along trajectories past the black hole, the numerical set-up is of 2 superposed flavour fields, evolved indirectly as a rotation from their mass eigenstates.

The mass eigenstate fields being directly simulated are each set up as a complex plane wave. At each point, the state in the flavour basis is a rotation of these two mass states, as the inverse of equation (72). The initial state is purely in one flavour, and at later times the oscillation probability at a point can be calculated as the square of the overlap of the fields with the other flavour eigenstate.

As mentioned in the previous section, these simulations are carried out in Cartesian Kerr-Schild coordinates, given in section 2 of [20]. As expected on a fixed background, the gauge choices for the lapse and shift (equations (13) to (15) of [20]) are constant, i.e., $\partial_t \alpha = \partial_t \beta^i = 0$.

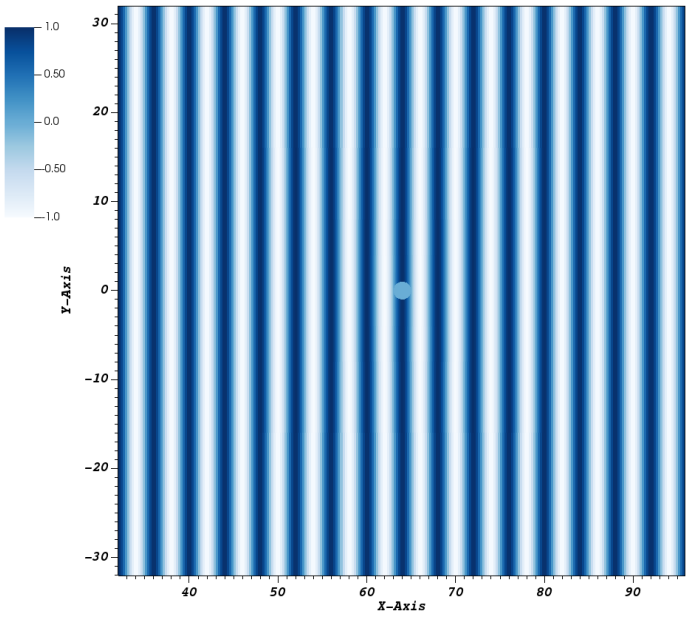

Figure 6: This image shows the initial state of the real part of a mass eigenstate field, with the black hole in the centre. The total amplitude of the field is initially constant everywhere, but the real and imaginary components oscillate sinusoidally in the x direction.

5.3 Initial conditions

Since the mass eigenstates obey the Klein-Gordon equation (equation (40)), the initial state of each mass eigenstate field is given by the diagonal values of equation (74) with time $t = 0$. This corresponds to the real and imaginary parts of each field oscillating

sinusoidally along the direction of propagation, with the wavelength given by $2\pi/k_m$. The two momenta are assumed to be roughly equal, i.e., $k_{m_1} \approx k_{m_2} = k_m$. This would be expected of highly relativistic states produced by the same source. An example for this initial state is shown in figure 6.

To obtain an initial state entirely of one flavour, the amplitude of the two massive fields, ϕ_{m_1} and ϕ_{m_2}, are proportional to $\cos(\alpha)$ and $-\sin(\alpha)$ respectively. This state is clearly orthogonal to the flavour eigenstate b (again of equation (72)).

5.4 Parameters

The main parameters that can be altered in these simulations are the black hole mass and angular momentum, and the mass eigenstate fields' momenta and masses. The mixing angle can also be varied, but as implied by equations (75) and (117) this only changes the amplitude of the probability oscillations.

In numerical simulations it is important to consider the various length scales involved in the problem. These scales correspond roughly to the sizes of the important features, and if they differ significantly it becomes computationally expensive to resolve all the features simultaneously. In this case, there are four important scales — the black hole Schwarzschild radius $R_S \approx 2M$, the scalar field wavelength, the flat-space oscillation length (equation (118)), and the oscillation length in the orthoradial direction — this is best seen in the various figures in section 5 below.

As mentioned in section 5.1, the length scale in the units used here is not fixed. As a result, the physical interpretation of the following results is usefully ambiguous. This makes them equally valid, for example, for any reasonable black hole mass — provided that all other values are scaled accordingly. In this work, the black hole's mass has been fixed at a value of 0.5, so that each unit of length corresponds to one Schwarzschild radius.

5.5 Previous results

The first target of the numerical simulations is to reproduce the general features in the results of [1]. This is both to ensure that the simulation is functioning as expected, and to

give a starting point for comparisons with new findings. Unlike in [1], where masses have been chosen that differ by 1%, masses have been chosen here that differ by 10%. While this precludes the possibility of a direct comparison, it leads to oscillation patterns with much greater variation, and flat-space oscillation lengths much closer to the other length scales involved. Figure 7 shows a comparison of the results found here with the results in [1]. Here, $R_S = 1$, which is equivalent to the length scales in this simulation being half those used in [1].

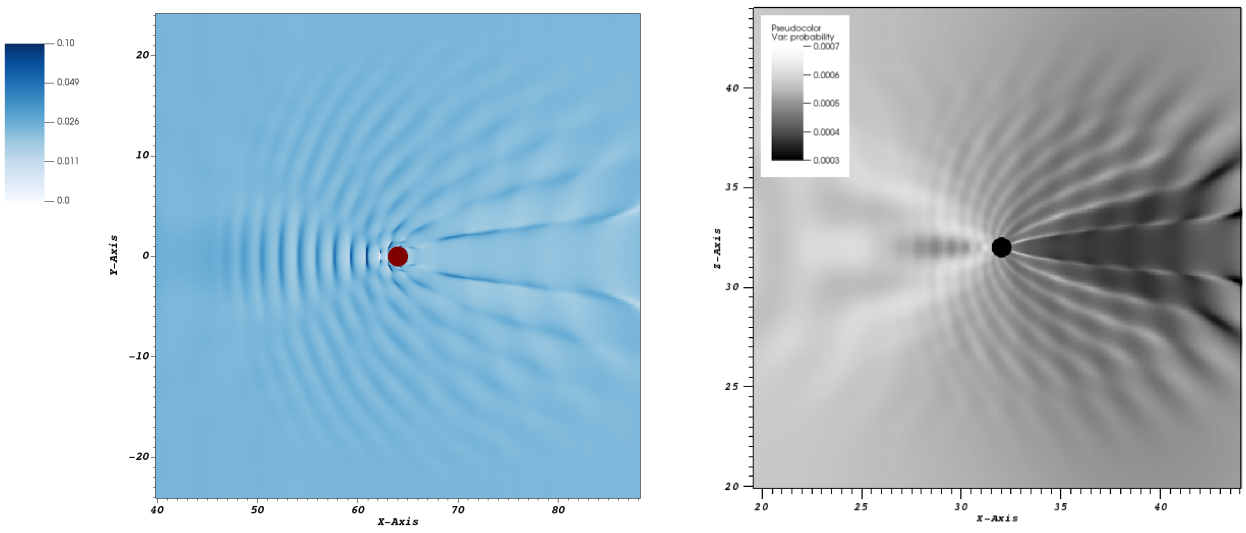

Figure 7: The left hand side shows the new oscillation pattern obtained for a percentage mass difference of 10%. The right hand side shows the pattern found in [1] for a mass difference of 1%.

These figures clearly show a similar pattern, with a parabolic structure along lines of equal probability. Observation of the radial oscillations in the analytic results is not expected here, as the whole field (far from the black hole) oscillates roughly 'together' in time. This is in contrast with the particle picture, where the (proper) distance from the source is correlated with the time a particle has taken to get there.

While these general features have already been analysed in the previous work, the aim of the following sections is to evaluate the numerical results more closely — to study a wider range of parameters, and to isolate the effects of varying these parameters. This will be guided by the analytic results of section 3, but those results are not expected to directly predict the patterns observed here, due to the fundamental differences between

the particle and field pictures. Finally, results will be given for black holes with non-zero angular momentum.

5.6 Isolation of mass variables

By rewriting the product of cosines in equation (117) as

$$\cos\left(\frac{m_+^2\Delta b^2}{8kr}\right)\cos\left(\frac{m_-^2\Delta b^2}{8kr}\right) = \frac{1}{2}\left(\cos\left(\frac{\Delta m^2\Delta b^2}{8kr}\right) + \cos\left(\frac{\Sigma m^2\Delta b^2}{8kr}\right)\right) \tag{123}$$

it becomes clear that the effect of the particle masses on the oscillation pattern is best understood through Δm^2 and Σm^2, rather than the individual masses. As a result, the following sets of simulations have been chosen to isolate each of these variables.

Figure 8 shows these results for a fixed Σm^2 and different values of Δm^2, while figure 9 shows the reverse. In both figures, subfigure (a) corresponds to $\Sigma m^2 = 0.75$ and $\Delta m^2 = 0.75$. Both figures also have fixed black hole masses of 0.5 and momenta $k = \frac{\pi}{2R_s}$.

It is clear that in both of these figures, the patterns are very similar. The only non-trivial difference in figure 8 (with Δm^2 varied) is a change in the scale of the oscillation pattern, with the amplitudes in (c) roughly a tenth of those in (a). The difference in the background (far-distance) probability is likely due to the expected change in oscillation time, leading to different phases in the background probability at a given time.

The lack of variation in the orthoradial oscillations implies that these oscillations have a fundamentally different origin to those predicted analytically. This may be a result of the approximations made in calculating the analytic results, or of the differences between the particle and field pictures.

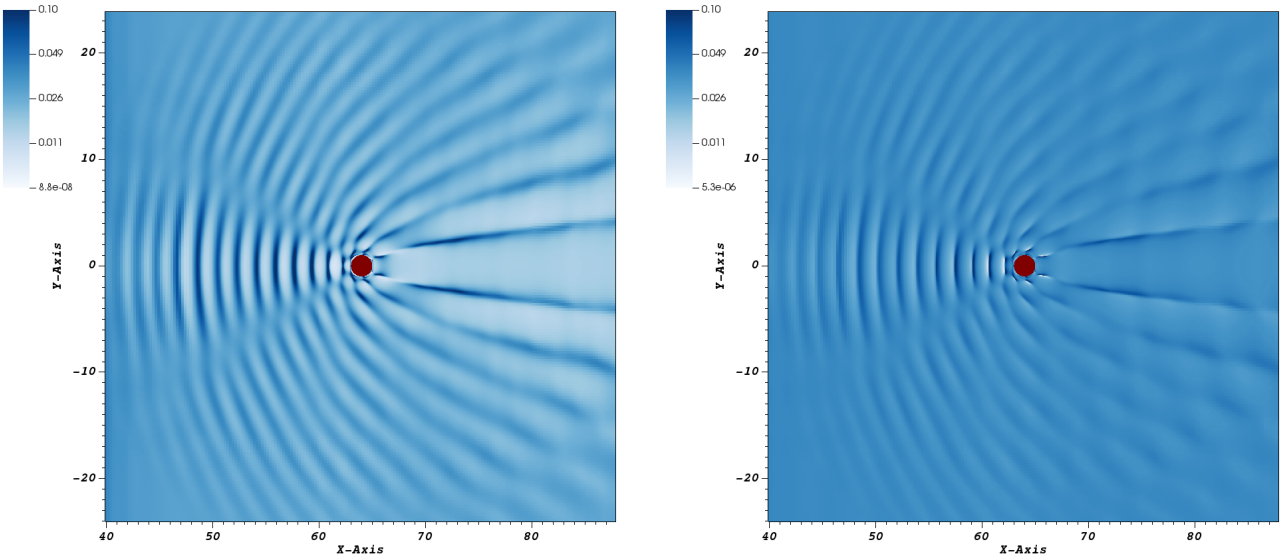

(a) $\Delta m^2 = 0.75$

(b) $\Delta m^2 = 0.25$

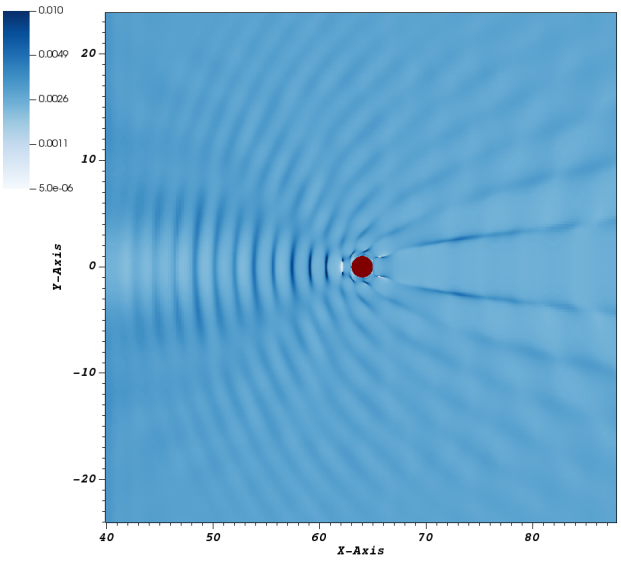

(c) $\Delta m^2 = 0.05$

Figure 8: Oscillation patterns for a fixed $\Sigma m^2 = 1.25$ and different values of Δm^2. In all figures, time T = 40, the black hole mass M = 0.5 and the particle momentum $k = \frac{\pi}{2R_s}$.

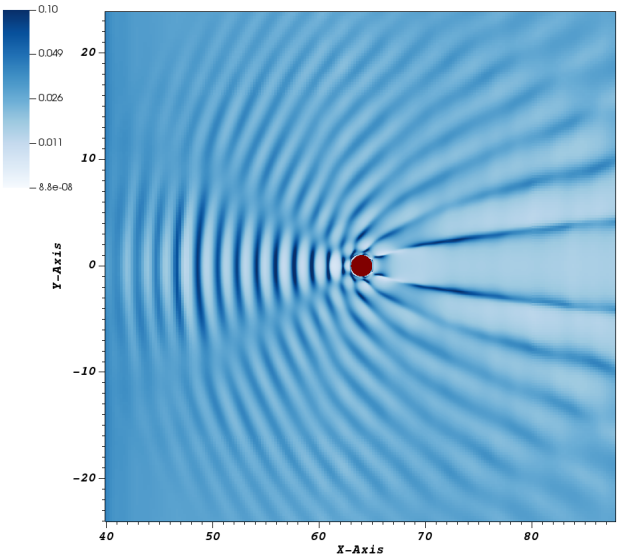

(a) $\Sigma m^2 = 1.25$

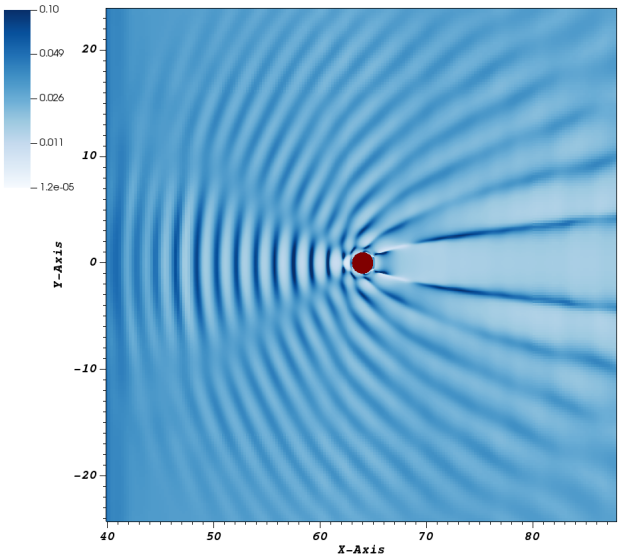

(b) $\Sigma m^2 = 2.75$

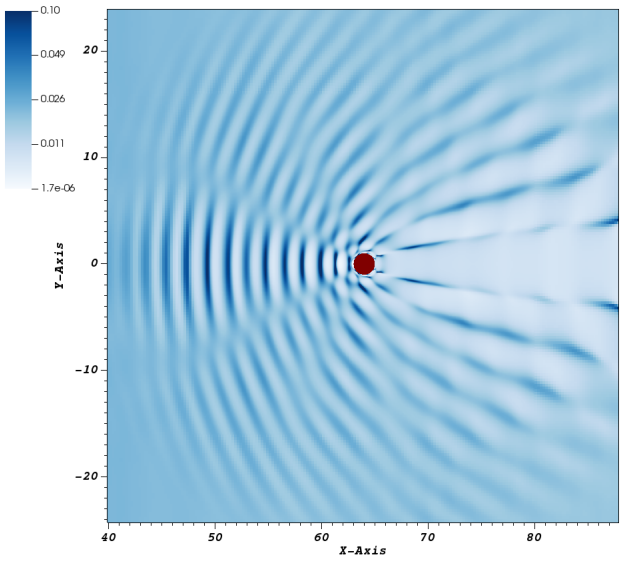

(c) $\Sigma m^2 = 0.85$

Figure 9: Oscillation patterns for a fixed $\Delta m^2 = 0.75$ and different values of Σm^2. In all figures, time T = 40, the black hole mass M = 0.5 and the particle momentum $k = \frac{\pi}{2R_s}$.

5.7 Isolation of momentum

Referring again to equation (117), it is expected that varying the momentum k (or, equivalently, the width of the initial wave) will greatly affect the oscillation pattern. Since the momentum appears in the denominator of all the terms, increasing the momentum should decrease the oscillation lengths in both the radial and orthoradial directions. Figure 10 shows the oscillation pattern for three values of the momentum.

Evidently, the expectation described above is strongly supported by these results — a decrease in the momentum leads to an increase in at least the orthoradial oscillation length. While the results of the previous section suggest an alternative, unknown origin for these orthoradial oscillations, this result at least shows that they are inversely dependent on the particle momentum. This finding agrees with that in Figure 3 of [1], where two different momenta are compared.

5.8 Results for Kerr black holes

The final parameter to be adjusted is a, which describes the angular momentum per unit mass of the black hole. The value of a cannot exceed M (the black hole mass) [4], so with $M = 0.5$ here, a is chosen to equal 0.4. The oscillation pattern for these parameters is shown at various scales in figure 11.

While it has been shown in section 3 that the first-order contribution of the spin to the phase difference cancels out, the relationship between the two impact parameters and the intersection point has not been investigated in the Kerr case. However, it is intuitively expected that increasing a will 'rotate' the intersection point of two incoming particles, with respect to these coordinates. This effect is also expected to drop off sharply as the radius increases, which is clearly observed in figure 11.

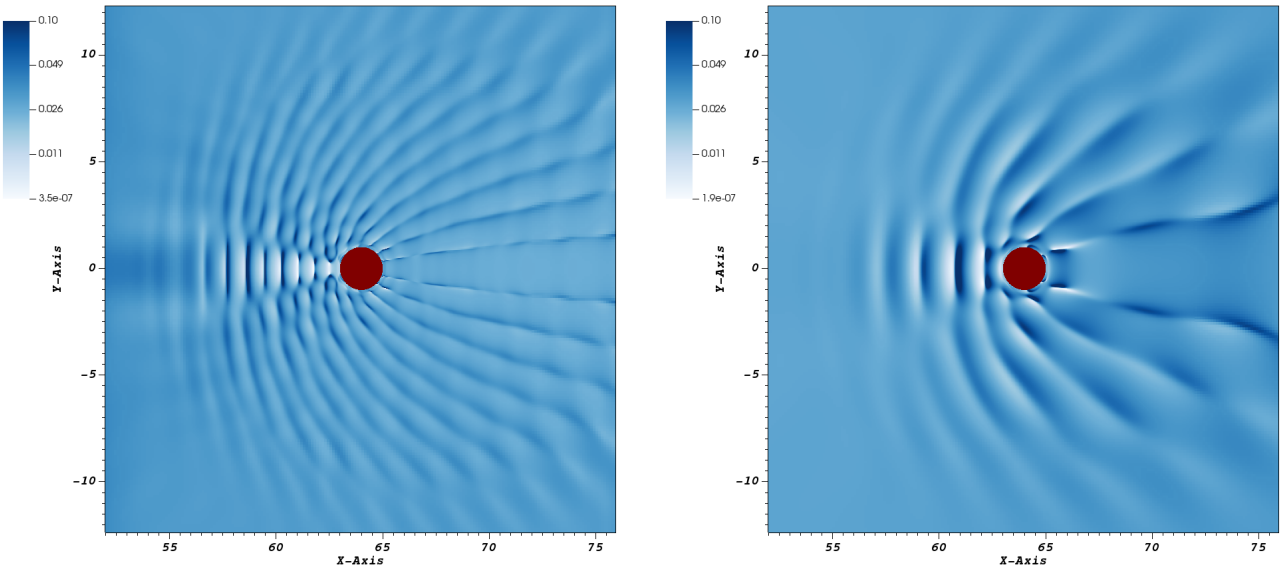

(a) $k = \frac{\pi}{R_s}$ (b) $k = \frac{\pi}{2R_s}$

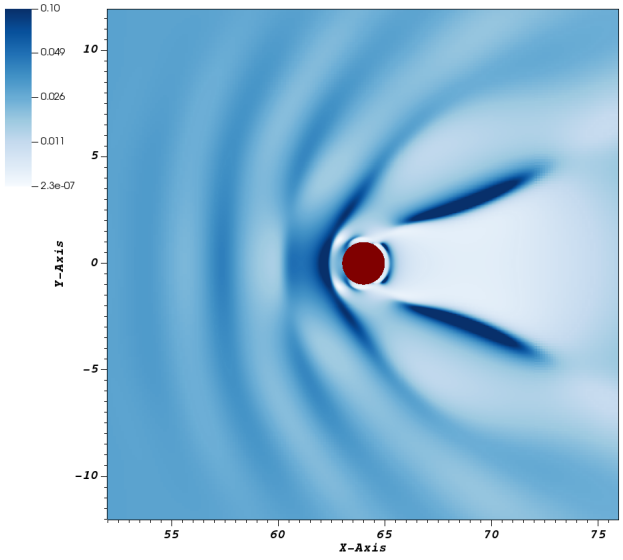

(c) $k = \frac{\pi}{4R_s}$

Figure 10: Oscillation patterns for various values of the particle momentum k. In all figures, the particle masses are fixed as $\Delta m^2 = 0.75$ and $\Sigma m^2 = 1.25$, with time T = 40 and the black hole mass M = 0.5

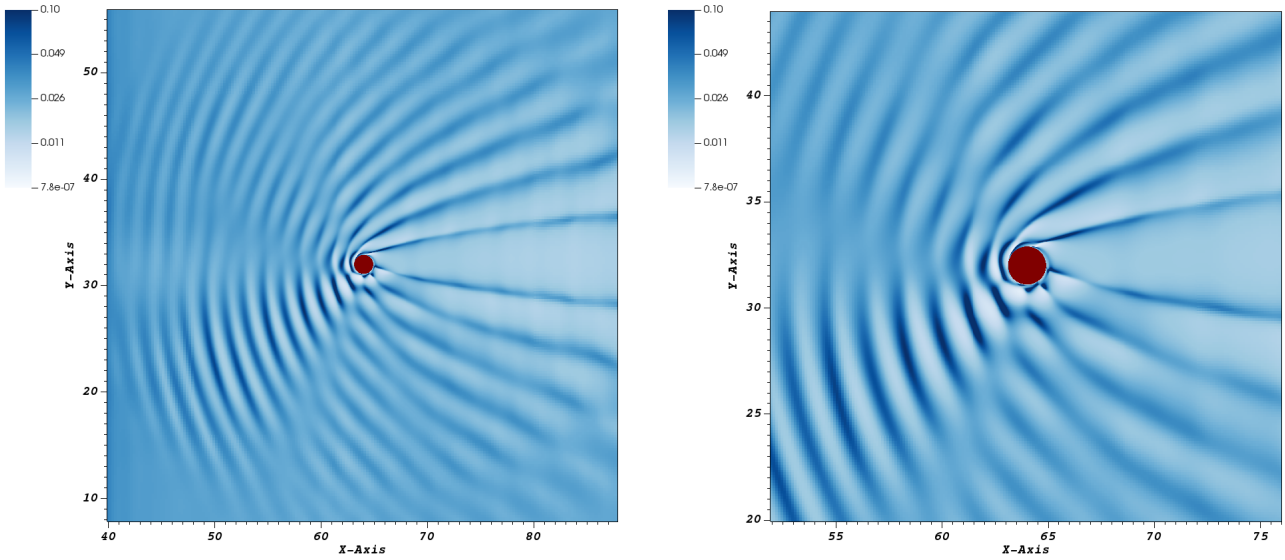

Figure 11: The oscillation pattern for a black hole with spin per unit mass $a = 0.4$, black hole mass $M = 0.5$, and particle masses with $\Delta m^2 = 0.75$ and $\Sigma m^2 = 1.25$. The time $T = 40$, and two different scales are shown (with the figure on the right having half the side length of that on the left.

6 Conclusions and future developments

The background, analysis and results presented here have laid the groundwork for future numerical research into flavour oscillations. The 3+1 decomposition has been explored, with various formulations culminating in the CCZ4 equations that are used in the GR-Chombo code. The general features of numerical relativity codes have also been explored, and some specific features of the GRChombo code (such as AMR) that are used for efficient simulations of dynamical backgrounds have been described.

While the full simulation of flavour oscillations on dynamical backgrounds has not yet been carried out, the first results have been obtained for simpler fixed background scenarios, and comparisons have been made with previous work.

Analytic results for this scenario in [2] have been extended to include low-spin Kerr black holes, and the expression for black hole scattering has been fully derived with the ambi-

guities in [2] clarified. This has allowed for a comparison between these equations and the results of the aforementioned simulations. The oscillations patterns obtained here and in [1] do not appear to have the mass dependencies predicted by the analytic expressions, but do appear to depend strongly on the momentum (as predicted).

This mismatch between the predictions and results calls for further investigations of this scenario. A remodelling of the initial conditions could be used to study an incoming wave packet rather than an infinite plane wave, and this may mitigate some of the differences between the field and particle pictures. This would also allow for a more thorough investigation of the radial oscillations, which are not clearly captured by the current results.

Beyond this, the CCZ4 formalism and the GRChombo numerical relativity code can now be used to consider more exotic physical scenarios, such as scattering by black hole binary systems. A more realistic comparison to neutrino oscillations could also be obtained by introducing a third flavour (mass) field.

References

[1] J. Alexandre and K. Clough, "Black hole interference patterns in flavor oscillations," *Phys. Rev. D*, vol. 98, p. 043004, Aug 2018.

[2] N. Fornengo, C. Giunti, C. W. Kim, and J. Song, "Gravitational effects on the neutrino oscillation," *Phys. Rev. D*, vol. 56, pp. 1895–1902, Aug 1997.

[3] S. Mertens, "Direct Neutrino Mass Experiments," *J. Phys. Conf. Ser.*, vol. 718, no. 2, p. 022013, 2016.

[4] R. M. Wald, *General Relativity*. Chicago, USA: Chicago Univ. Pr., 1984.

[5] J. Jost, *Riemannian Geometry and Geometric Analysis*, 7th ed. Springer Cham, 1984.

[6] S. M. Carroll, *Spacetime and Geometry*. Cambridge University Press, 7 2019.

[7] T. W. Baumgarte and S. L. Shapiro, *Numerical Relativity: Solving Einstein's Equations on the Computer*. Cambridge University Press, 2010.

[8] E. Gourgoulhon, *3+1 Formalism in General Relativity*. Springer Berlin, Heidelberg, 2012.

[9] T. W. Baumgarte and S. L. Shapiro, *Numerical Relativity: Starting from Scratch*. Cambridge University Press, 2 2021.

[10] K. Clough, P. Figueras, H. Finkel, M. Kunesch, E. A. Lim, and S. Tunyasuvunakool, "GRChombo : Numerical Relativity with Adaptive Mesh Refinement," *Class. Quant. Grav.*, vol. 32, no. 24, p. 245011, 2015.

[11] O. A. Reula, "Hyperbolic methods for Einstein's equations," *Living Rev. Relativ. 1*, 1998.

[12] O. Sarbach, G. Calabrese, J. Pullin, and M. Tiglio, "Hyperbolicity of the BSSN system of Einstein evolution equations," *Phys. Rev. D*, vol. 66, p. 064002, 2002.

[13] C. Gundlach, J. M. Martin-Garcia, G. Calabrese, and I. Hinder, "Constraint damping in the Z4 formulation and harmonic gauge," *Class. Quant. Grav.*, vol. 22, pp. 3767–3774, 2005.

[14] D. Alic, C. Bona-Casas, C. Bona, L. Rezzolla, and C. Palenzuela, "Conformal and covariant formulation of the Z4 system with constraint-violation damping," *Phys. Rev. D*, vol. 85, p. 064040, 2012.

[15] Y. Choquet-Bruhat and T. Ruggeri, "Hyperbolicity of the 3+1 system of Einstein equations," *Commun. Math. Phys.*, vol. 89, pp. 269–275, 1983.

[16] C. Bona, J. Masso, E. Seidel, and J. Stela, "A New formalism for numerical relativity," *Phys. Rev. Lett.*, vol. 75, pp. 600–603, 1995.

[17] J. G. Baker, J. Centrella, D.-I. Choi, M. Koppitz, and J. van Meter, "Gravitational wave extraction from an inspiraling configuration of merging black holes," *Phys. Rev. Lett.*, vol. 96, p. 111102, 2006.

[18] D. Piriz, M. Roy, and J. Wudka, "Neutrino oscillations in strong gravitational fields," *Phys. Rev. D*, vol. 54, pp. 1587–1599, 1996.

[19] A. Ashtekar, "Asymptotic Structure of the Gravitational Field at Spatial Infinity," in *General Relativity and Gravitation II*, A. Held, Ed., vol. 2, Jan. 1980, p. 37.

[20] R. A. Matzner, M. F. Huq, and D. Shoemaker, "Initial data and coordinates for multiple black hole systems," *Phys. Rev. D*, vol. 59, p. 024015, 1999.

[21] S. Strogatz, *Nonlinear Dynamics and Chaos: With Applications to Physics, Biology, Chemistry, and Engineering*, 2nd ed. CRC Press, 2015.

[22] Y. Zlochower, J. G. Baker, M. Campanelli, and C. O. Lousto, "Accurate black hole evolutions by fourth-order numerical relativity," *Phys. Rev. D*, vol. 72, p. 024021, 2005.

[23] M. Berger and I. Rigoutsos, "An algorithm for point clustering and grid generation," *IEEE Transactions on Systems, Man and Cybernetics*, vol. 21, no. 5, pp. 1278–1286, 1991.

[24] H. O. Kreiss and J. Oliger, "Comparison of accurate methods for the integration of hyperbolic equations," *Tellus*, vol. 24, no. 3, pp. 199–215, 1972.